

ADA102613

LEVEL

62

AD

TECHNICAL REPORT ARBRL-TR-02334

A DETAILED COMPARISON OF 3-D HYDROCODE
COMPUTATIONS FOR SHOCK DIFFRACTION LOADING
ON AN S-280 ELECTRICAL EQUIPMENT SHFLTER

Richard E. Lottero

June 1981

DTIC
ELECTRONIC
AUG 10 1981
S C



US ARMY ARMAMENT RESEARCH AND DEVELOPMENT COMMAND
BALLISTIC RESEARCH LABORATORY
ABERDEEN PROVING GROUND, MARYLAND

Approved for public release; distribution unlimited.

818 10 014

Destroy this report when it is no longer needed.
Do not return it to the originator.

Secondary distribution of this report by originating
or sponsoring activity is prohibited.

Additional copies of this report may be obtained
from the National Technical Information Service,
U.S. Department of Commerce, Springfield, Virginia
22161.

The findings in this report are not to be construed as
an official Department of the Army position, unless
so designated by other authorized documents.

This report is made available to manufacturers' agents in this country
and does not constitute endorsement of any commercial product.

UNCLASSIFIED

SECURITY CLASSIFICATION OF THIS PAGE (When Data Entered)

REPORT DOCUMENTATION PAGE		READ INSTRUCTIONS BEFORE COMPLETING FORM
1. REPORT NUMBER TECHNICAL REPORT ARBRL-TR-02334	2. GOVT ACCESSION NO. AD-A102 613	3. RECIPIENT'S CATALOG NUMBER
4. TITLE (and Subtitle) A DETAILED COMPARISON OF 3-D HYDROCODE COMPUTATIONS FOR SHOCK DIFFRACTION LOADING ON AN S-280 ELECTRICAL EQUIPMENT SHELTER	5. TYPE OF REPORT & PERIOD COVERED Final Oct 78 - Dec 80	6. PERFORMING ORG. REPORT NUMBER
7. AUTHOR(s) Richard E. Lottero	8. CONTRACT OR GRANT NUMBER(s)	
9. PERFORMING ORGANIZATION NAME AND ADDRESS US Army Ballistic Research Laboratory ATTN: DRDAR-BLT Aberdeen Proving Ground, MD 21005	10. PROGRAM ELEMENT, PROJECT, TASK AREA & WORK UNIT NUMBERS 1L162120AH25, and 1L66261AH26 84H	
11. CONTROLLING OFFICE NAME AND ADDRESS US Army Armament Research & Development Command US Army Ballistic Research Laboratory ATTN: DRDAR-BL, APC, MD 21005	12. REPORT DATE JUNE 1981	13. NUMBER OF PAGES 104
14. MONITORING AGENCY NAME & ADDRESS (if different from Controlling Office) US Army Electronics Research & Development Command US Army Harry Diamond Laboratories ATTN: DELHD-NP Adelphi, MD 20783	15. SECURITY CLASS. (of this report) UNCLASSIFIED	15a. DECLASSIFICATION/DOWNGRADING SCHEDULE
16. DISTRIBUTION STATEMENT (of this Report) Distribution unlimited, approved for public release.		
17. DISTRIBUTION STATEMENT (of the abstract entered in Block 20, if different from Report)		
18. SUPPLEMENTARY NOTES		
19. KEY WORDS (Continue on reverse side if necessary and identify by block number) Shock diffraction BAAL Finite difference Hydrocode S-280 Shelter NULL		
20. ABSTRACT (Continue on reverse side if necessary and identify by block number) (bas) / The normal shock diffraction loading on an S-280 Electrical Equipment Shelter (essentially a rectangular parallelepiped) by a 34.5 kPa (5.0 psi) shock is reported. Two different three-dimensional hydrodynamic computer codes, BAAL from the Los Alamos Scientific Laboratory and NULL from the Air Force Weapons Laboratory, were used. The results from the two hydrocodes are compared with one another, showing good agreement, and with two existing semiempirical models. Improvements to these models are suggested, as the computed results indicate that the		

UNCLASSIFIED

SECURITY CLASSIFICATION OF THIS PAGE(When Data Entered)

net loading for this three-dimensional shelter is significantly lower than the models predict. The effects of artificial viscosity in the hydrocodes and of the smearing of the computational shock in the finite difference grid are also discussed.

UNCLASSIFIED

SECURITY CLASSIFICATION OF THIS PAGE(When Data Entered)

TABLE OF CONTENTS

	Page
LIST OF ILLUSTRATIONS.	5
LIST OF TABLES	7
I. INTRODUCTION	9
II. REFERENCE PROBLEM.	10
A. Target	10
B. Shock and Ambient Conditions	10
C. One-Dimensional Check.	10
III. SEMIEMPIRICAL MODELS	12
A. Background	12
B. Technical Manual	12
1. Front Face	12
2. Back Face.	15
3. Top and Side Faces	15
C. Taylor's Model	17
1. Front Face	17
2. Back Face.	21
3. Top and Side Faces	21
IV. HYDROCODES	21
A. Background	21
B. BAAL	22
C. HULL	23
V. HYDROCODE COMPUTATIONS	24
VI. LOADING ON SHELTER FACES	27
A. Remarks.	27
B. Front Face	27
C. Back Face.	31
D. Top Face	33
E. Side Face.	35

Accession For	
NTIS GRAI	
DTIC TAB	
Unannounced	
Justification	
By	
Distribution	
Availability Codes	
Avail and/or	
Dist. Specifi	
A	

TABLE OF CONTENTS (Continued)

	Page
VII. NET LOADING.	35
A. Definition	35
B. Discussion	35
VIII. ROTATIONAL MOMENT.	37
IV. CONCLUSION	42
REFERENCES	45
APPENDICES	
A - SOLUTION FOR SHOCK TUBE WITH CLOSED END	47
B - DETAILED DISCUSSION OF SEMIEMPRICAL MODELS	51
C - COMPUTATIONAL GRIDS	57
D - OTHER LOADING FUNCTIONS	63
E - DETAILED COMPARISON OF HYDROCODE RESULTS.	71
LIST OF SYMBOLS.	91
DISTRIBUTION LIST.	93

LIST OF ILLUSTRATIONS

Figure	Page
1. Simplified one-dimensional flow field.	11
2. Front and back face average overpressure	14
3. Average pressure difference, front face minus back face. . .	16
4. Top face average overpressure.	18
5. Side face average overpressure	19
6. S-280 Electrical Equipment Shelter in the computational flow field	25
7. Front face average overpressure.	28
8. Back face average overpressure	32
9. Height of center-of-overpressure on front face	38
10. Height of center-of-overpressure on back face.	39
11. Net rotational moment due to overpressure.	41

LIST OF TABLES

I. INTRODUCTION

The loading on equipment and structures caused by shock diffraction and drag have been of particular interest to the Army ever since the introduction of nuclear weapons. Because of the inherent three-dimensional (3-D) nature of such loading, the more commonly accepted method for ascertaining this loading has been through field testing, dating from atmospheric nuclear tests to current tests of large-scale high explosives. Because of the high cost and necessarily complex planning involved, these tests are held infrequently. Unpredictable anomalies such as jetting frequently occur, often with the intended targets receiving loadings considerably different from that which had been expected. Space for targets and data acquisition equipment is invariably at a premium during these tests, leaving potentially valuable tests untried, and worthwhile data ungathered.

As pointed out by Taylor¹ in 1972, the accepted methods for computing shock diffraction loading on simple structures as outlined in the US Army Technical Manual TM-5-856-1², hereinafter referred to as the Technical Manual, are no longer sufficiently accurate for studies in blast hardening and vulnerability assessment. The models outlined in the Technical Manual treat a given 3-D structure, such as a rectangular parallelepiped, as being locally two-dimensional. Loading is then computed based on the speed at which a rarefaction wave travels across a characteristic dimension of the given target face. During the last several years, numerical methods in the form of hydrodynamic computer codes (hydrocodes) for simulating 3-D shock diffraction over obstacles have been advanced to the point where they can be used to complement and, in some cases, replace the use of experiments and models such as those in the Technical Manual.

The objective of the present work is to illustrate the capabilities of two hydrocodes for predicting shock diffraction loading and to compare them with two semiempirical models. The hydrocodes used for the comparisons are HULL and BAAL. One semiempirical model is that from the Technical Manual, and the other is an improved model suggested by Taylor¹.

A reference problem is defined: the S-280 Electrical Equipment Shelter struck by a 34.5 kPa (5.0 psi) overpressure step shock. Improvements to the models for determining loading in the Technical

¹W. J. Taylor, "A Method for Predicting Blast Loads During the Diffraction Phase," *The Shock and Vibration Bulletin*, NP. 42, Part 4 of 5, Shock and Vibration Center, Naval Research Laboratory, Washington, DC, p. 135 (Jan 72).

²"Design of Structures to Resist the Effects of Atomic Weapons," US Army Corps of Engineers EM-1110-345-413, 1 July 1959, (UNCLASSIFIED). (Republished as TM5-856-1 in 1965.)

Manual are suggested; these improved models give good agreement with the hydrocode results. The BAAL hydrocode has previously been shown to compare well with experimental shock loading on a similar rectangular parallelepiped at the same shock strength. Finally, a discussion is presented on the net rotational moments on the shelter as predicted by the several methods.

II. REFERENCE PROBLEM

A. Target

The target is an S-280 Electrical Equipment Shelter (hereinafter referred to as the shelter), 3.62 m wide, 2.17 m deep, and 2.11 m high. The shelter is sitting on the ground with one of the larger of the two different sized faces, defined here as the front face, oriented so that it is normal to the velocity vector of an oncoming one-dimensional (1-D) shock wave.

B. Shock and Ambient Conditions

The shock wave is a step shock with an overpressure $p^* = 34.5$ kPa (5.0 psi). Ambient conditions ahead of the shock are temperature $T_1 = 288.2^\circ\text{K}$ (518.7°R), pressure $p_1 = 101.3$ kPa (14.7 psi), and density $\rho_1 = 1.225 \text{ kg/m}^3$ (.0765 lbm/ft³). The air both ahead of and behind the shock is assumed to be a polytropic gas, with a ratio of specific heats $\gamma = 1.4$. Throughout the remainder of this report, the interaction of this shock wave with the shelter described above will frequently be referred to as "the present case."

C. One-Dimensional Check

A simplified, locally 1-D model that can be used to represent the flow field at the time that the incident shock reflects from the shelter's front face is shown in Figure 1. The flow field shown is for a shock tube with a closed end. Region 1 represents the ambient air; region 2, the air behind the incident shock wave; region 3, the shock tube reservoir; and region 4, the accelerated flow region between the expansion wave and the contact surface. Finally, region 5 is the region behind the shock wave which reflected off the rigid wall that represents the shelter's front face. The subscripts used with flow field variables in this report indicate the particular region of interest.

The values of the flow field variables for the 1-D check can be calculated from the shock tube relations with the shock and ambient conditions specified above. These 1-D variables are summarized in the table in Appendix A. The theoretical value of the peak reflected overpressure of 78.5 kPa calculated with the 1-D model is an excellent

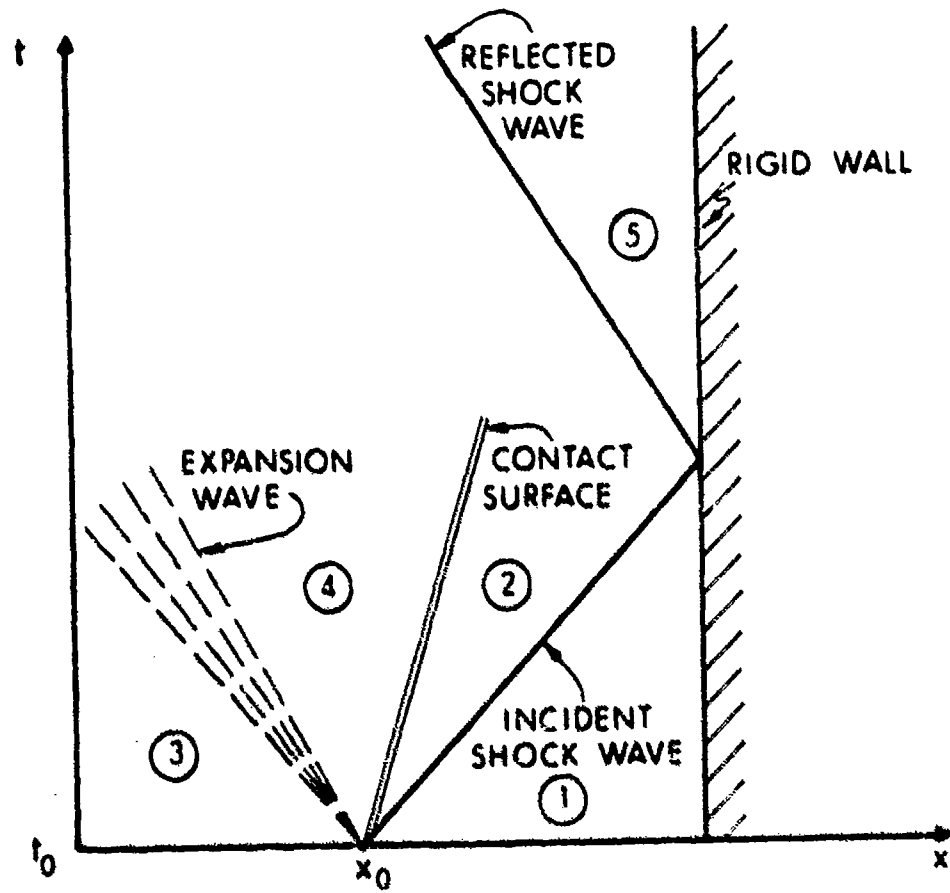


Figure 1. Simplified one-dimensional flow field.

reference point to use in assessing the validity of the hydrocode solutions of the real 3-D case. The initial reflection process at any given point on the front face is 1-D until the expansion waves coming in from the top and side edges of the front face arrive at that point.

III. SEMIEMPIRICAL MODELS

A. Background

Prior to presenting the results of the hydrocode computations, it is worthwhile to discuss the existing semiempirical models used to determine shock loading on 3-D structures. This allows not only a comparison between the loading predicted by the models, but also allows later comparison to the loading predicted by the hydrocodes. The chosen semiempirical models are (1) those from the Technical Manual², and (2) the improved models suggested by Taylor¹.

B. Technical Manual

The equations presented here are for a step shock, and any mention of the terms "shock" or "shock wave" in the following discussion are to be construed as referring to a step shock unless specifically noted to be otherwise. The semiempirical models in the Technical Manual are for decaying shock waves, but the relations can be easily modified to relate to step shocks. The derivations of the step shock equations from the decaying shock wave equations in the Technical Manual are given in Appendix B.

The Technical Manual models of interest here assume that the shock wave strikes a rectangular parallelepiped with the velocity vector of the shock wave normal to one of the faces of the parallelepiped. That face is defined as the front face. A semiempirical model which shows the shock reflection and subsequent expansion wave interactions is given for the front face. A semiempirical model is given for the back face which shows the shock expansion around the 90-degree corners with the top and side faces. A combined model is given for the top and side faces, showing shock movement along those faces plus wave interactions from the front and back faces.

These models from the Technical Manual, modified for step shocks, are discussed below. The predictions made using these models are also discussed and presented for later comparison with other models and with the hydrocode results. Any numerical values such as sound speed, shock speed, or overpressure refer specifically to the interaction of the reference 34.5 kPa step shock with the shelter (the present case).

1. Front Face. The model in the Technical Manual for calculating the loading on the front face is based on an assumed clearing time t_c , where

$$t_c = \frac{3h}{c_5} . \quad (1)$$

Here, c_5 is the sound speed on the front face of the shelter after the shock has reflected from it; for the present case, $c_5 = 369.6$ m/s. The value to be used for h is the smaller of either the height of the shelter or one-half the width; for the present case, $h = 1.81$ m. This gives a clearing time for the shelter $t_c = 14.69$ ms, where t_c is "... the time required to clear the front wall of reflection effects."² During this time, the average overpressure on the front face, \bar{p}_f^* , decreases from the peak reflected overpressure to a value

$$\bar{p}_f^* = (p_2 - p_1) + 0.85 \frac{1}{2} \rho_2 u_2^2 . \quad (2)$$

Here, p_2 is the pressure behind the shock, ρ_2 is the density behind the shock, and u_2 is the particle velocity behind the shock. For the present case, the peak reflected overpressure on the front face is $(p_5 - p_1)$ or 78.5 kPa (11.4 psi), and \bar{p}_f^* is 37.9 kPa (5.49 psi); p_5 is the pressure behind the reflected shock. Figure 2 shows the history of the average overpressure on the front face of the shelter calculated using the model in the Technical Manual. The term "average overpressure" refers to a spatial average on the shelter face at a given point in time, or at a series of points in time. In the later discussions concerning the hydrocode computations, average overpressure means a weighted spatial average, with the weighting based on the areas of the flow-field cells adjacent to the shelter surface. The other data shown in Figure 2 for the front face will be discussed later.

2. Back Face. The time required for the incident shock wave to arrive at the plane of the back wall is

$$t_d = \frac{D}{W_i} , \quad (3)$$

where D is the shelter depth, and W_i is the velocity of the incident shock. For the present case, $D = 2.17$ m and $W_i = 386.8$ m/s, so $t_d = 5.616$ ms. The rise time² required for the average pressure on the back face to go from ambient at time t_d to its peak value is

$$(t_b)_{rise} = \frac{ah}{c_1} , \quad (4)$$

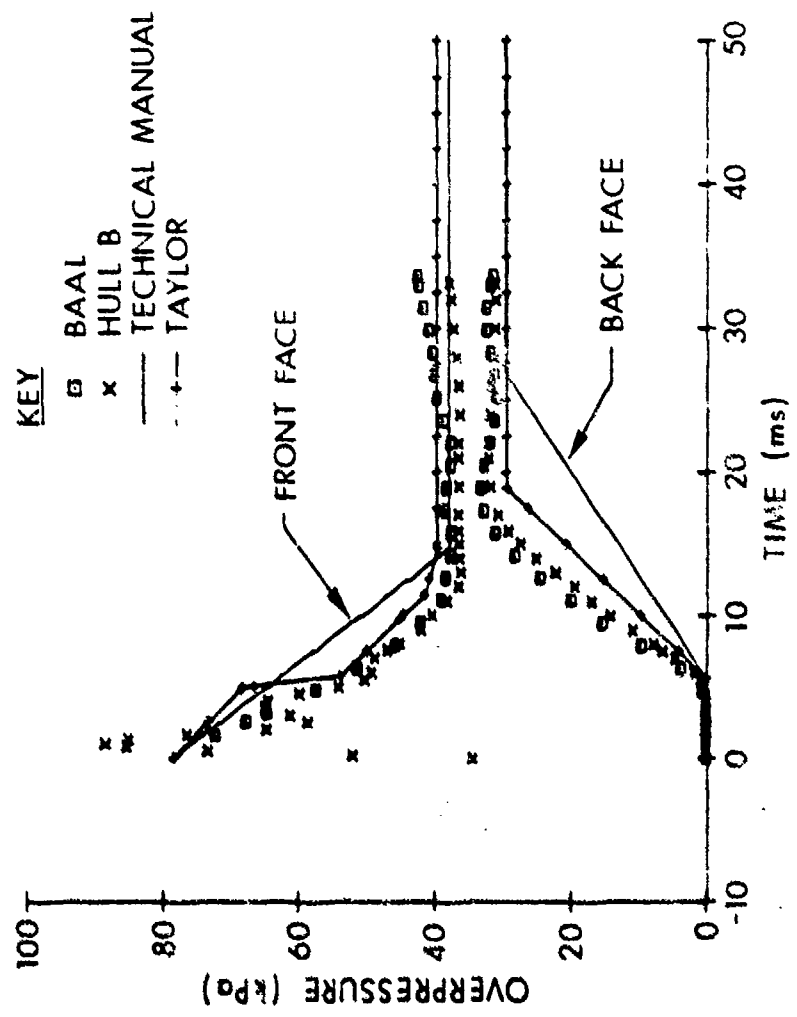


Figure 2. Front and back face average overpressure.

where $\alpha = 4.0$, c_1 is the sound speed ahead of the shock, and h is defined as before. Here, $h = 1.81$ m and $c_1 = 340.3$ m/s, so $(t_b)_{\text{rise}} = 21.28$ ms. The peak average overpressure² on the back face is

$$(\bar{p}_b^*)_{\text{max}} = \frac{1}{2} (p_2 - p_1) \left[1 + (1 - \beta) e^{-\beta} \right], \quad (5)$$

where

$$\beta = \frac{1}{2} \frac{(p_2 - p_1)}{p_1}, \quad (6)$$

or $(\bar{p}_b^*)_{\text{max}} = 29.3$ kPa.

Because the shock wave considered here is a step shock, the model in the Technical Manual implies that the average overpressure on the back face would remain at $(\bar{p}_b^*)_{\text{max}}$ indefinitely. The overpressure history calculated using this model is represented by the solid line labeled "BACK" in Figure 2.

Figure 3 shows the history of the average pressure difference between the front and back faces of the S-280 shelter using the Technical Manual model. The other data in Figures 2 and 3 will be discussed later.

3. Top and Side Faces. From the time $t = 0.0$ s, when the incident shock wave reaches the plane of the front face of the target, to the time t_d at which the shock wave reaches the plane of the back face, the average overpressure on the top face varies linearly³ from zero to

$$\bar{p}_{\text{top}}^* = (p_2 - p_1) \left[0.9 + 0.1 \left(1.0 - \frac{p_2 - p_1}{p_1} \right)^2 \right]. \quad (7)$$

For the present case, $\bar{p}_{\text{top}}^* = 32.5$ kPa at $t_d = 5.616$ ms. To account for vortex growth, shedding, and subsequent travel down the top face, the model predicts a local minimum in the average overpressure at the time

$$t_{\text{pmin}} = \frac{SD}{W_1}, \quad (8)$$

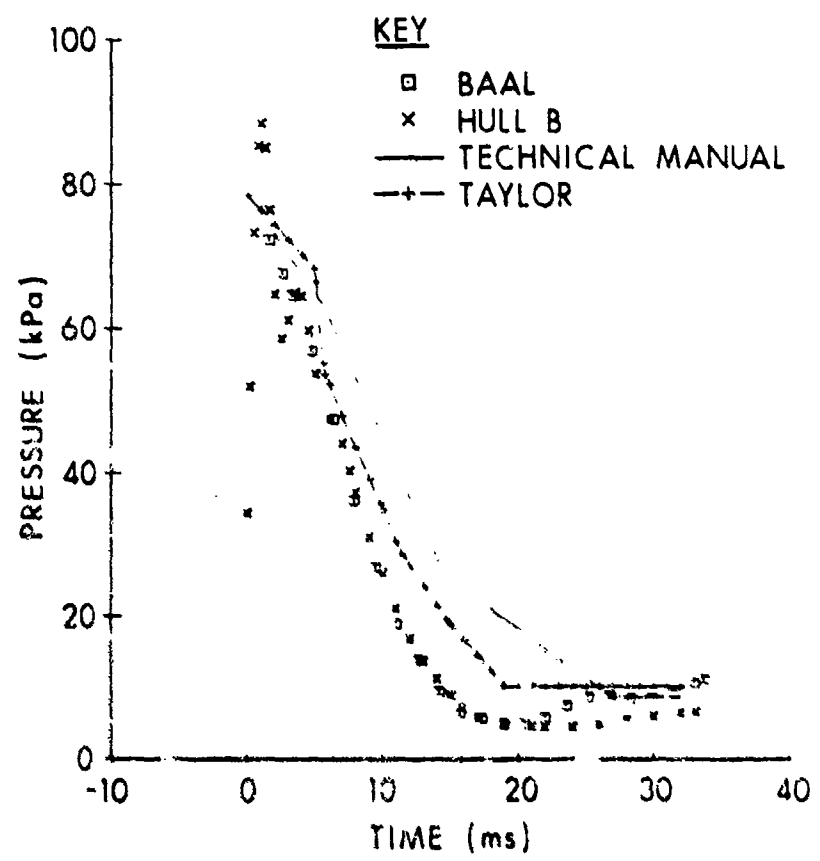


Figure 3. Average pressure difference, front face minus back face.

which for the present case is 28.08 ms. At that time, the average overpressure at the top face is calculated² as either

$$\bar{p}_{\text{top}}^* = (p_2 - p_1) \left[2.0 - \left(\frac{p_2 - p_1}{p_1} + 1 \right) \left(\frac{h}{D} \right)^{1/3} \right], \quad (9.1)$$

or

$$\bar{p}_{\text{top}}^* = (p_2 - p_1) \left[0.5 + 0.125 \left(2 - \frac{p_2 - p_1}{p_1} \right)^2 \right], \quad (9.2)$$

whichever is the lesser of the two. At this time, $\bar{p}_{\text{top}}^* = 25.2$ kPa for the present case. After this time, there is a linear rise in the average overpressure to a value

$$\bar{p}_{\text{top}}^* = p_2 - p_1, \quad (10)$$

from the time t_{pmin} to a time

$$t = t_{\text{pmin}} + \frac{15 D}{W_i}. \quad (11)$$

For the present case, $t = 98.28$ ms and $\bar{p}_{\text{top}}^* = 34.5$ kPa, the incident shock overpressure.

According to the method outlined in the Technical Manual, the geometry of the shelter is such that the times and average overpressures for the top face also apply directly to the side faces of the shelter. Figures 4 and 5 show the overpressure history for the top and side faces, respectively, of the shelter for the present case calculated with the above method. The hydrocode data and the proposed model shown in those figures will be discussed later.

C. Taylor's Model

1. Front Face. Taylor¹ suggested an alternate model to that of the Technical Manual to estimate the loading on the front face of an obstacle, based on the number of rarefaction wave crossings. For a 3-D object such as the shelter, there will be a succession of rarefaction waves originating from the top of the front face and reflecting from the bottom boundary, plus a succession of rarefaction waves originating from the side of the front face and reflecting from the symmetry plane. The reflected waves will also be rarefaction waves. In an actual occurrence of loading through shock diffraction, there

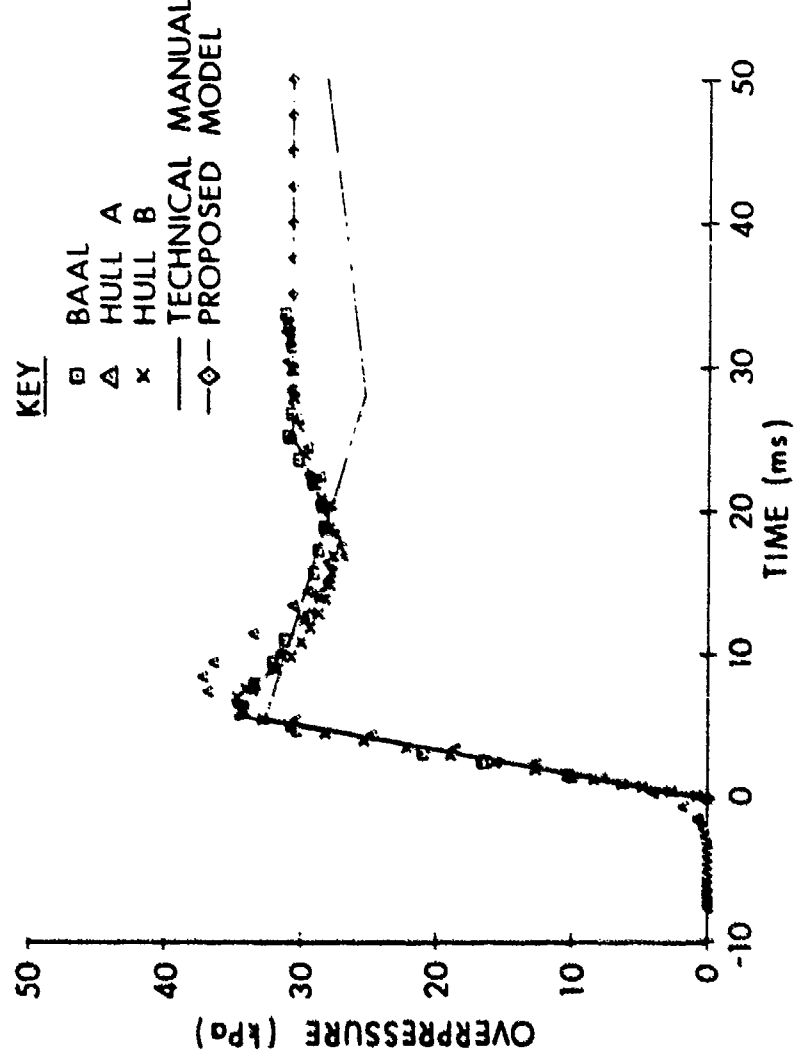


Figure 4. Top face average overpressure.

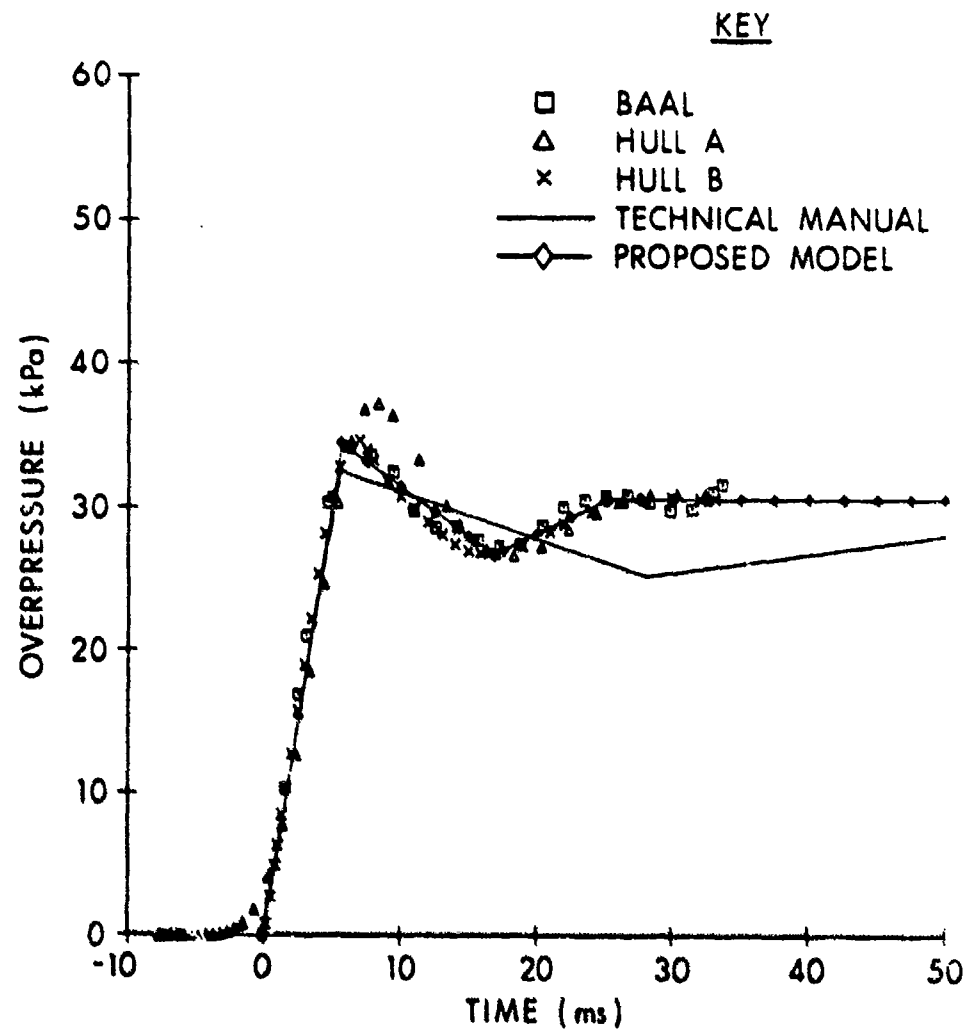


Figure 5. Side face average overpressure.

would be considerable interaction between the crossing expansion waves. Because Taylor intended that the model be a simple approximation, the waves are assumed not to interact with one another. As a further simplification, the rarefaction wave speeds are assumed to be equal to the sound speed in the reflection region immediately after the incident shock reflects from the front face.

Using Taylor's model, the required crossing time for an expansion wave running from the top to the bottom of the front face is 5.704 ms; for an expansion wave running between the side edge and the symmetry plane the crossing time is 4.897 ms. These times are based on a shelter height of 2.11 m, a one-half width of 1.81 m, and a sound speed $c_5 = 369.6$ m/s. For each expansion wave crossing, the average overpressure on the front face is then calculated as a percentage of the initial reflected overpressure on the front face. The values for average overpressure using Taylor's fitted curve¹ are summarized in Table 1 and shown in Figure 2.

TABLE 1. FRONT FACE AVERAGE OVERPRESSURE, TAYLOR'S MODEL

Time (ms)	Rarefaction Wave Number*	Wave Description	% Reflected Overpressure	Overpressure (kPa)
0.0	—	—	100.0	78.5
4.9	1	Side to Symmetry Plane	86.9	68.3
5.7	2	Top to Bottom	68.5	53.8
9.8	3	Symmetry Plane to Side	57.3	45.0
11.4	4	Bottom to Top	52.8	41.5
14.7	5	Side to Symmetry Plane	50.4	39.6

*Model stops at crossing number 5.

Taylor's model indicates a more rapid unloading of the front face during the diffraction phase than does the Technical Manual. (The diffraction phase on the front face lasts from the initial shock arrival until all wave interactions on that face have ended.) The two models are nearly the same for the drag phase on the front face ($t > 15$ ms). (The drag phase begins at the end of the diffraction phase for a given face.) The diffraction phase for the whole shelter ends when there

are no longer any wave interactions anywhere on the shelter; this ends at $t = 20$ ms. This and the hydrocode data shown in Figure 2 will be discussed later.

2. Back Face. Taylor's¹ data indicate that the constant α used in Equation (4) should be changed to 2.5 from 4.0. This gives a more rapid pressure rise time of 13.30 ms on the back face as compared with that calculated with the model in the Technical Manual. The overpressure history for the back face of the shelter calculated with Taylor's method is also shown in Figure 2. It shows much more rapid loading of the back face than does the Technical Manual model; the late-time loading is the same. Figure 3 shows the history of the average pressure difference between the front and back faces of the shelter using the models outlined by Taylor. The net loading predicted by Taylor's models is much less than that for the Technical Manual for nearly all of the diffraction phase. The hydrocode data shown in Figure 3 will be discussed in a later section.

3. Top and Side Faces. Taylor did not suggest an improved method for computing the average overpressure on the top and side faces of an object such as the shelter.

IV. HYDROCODES

A. Background

Until relatively recently, models such as those outlined in the Technical Manual were the accepted means for calculating the loading on a structure being struck by a shock wave. Taylor¹ pointed out the more serious deficiencies in the simple models being used, particularly the poor modeling of three-dimensional effects, and suggested a simple but effective model based on wave interactions. A more generalized version of Taylor's wave interaction model has since been adapted in the TRUCK code by Hobbs, et al.³ Two features of this model are the ability to model oblique loading and more complex target shapes.

However, it was apparent that a more general and accurate computational model than that offered by the simple models was needed. At the time of Taylor's¹ paper, hydrodynamic computer codes capable of solving the Euler equations (and in limited cases the Navier-Stokes equations) for two-dimensional flow were fairly well established. Advances were also being made in the development of hydrodynamic computer codes.

³N. P. Hobbs, J. P. Walsh, G. Zartarian, W. H. Lee, and Y. Wu, "TRUCK - A Digital Computer Program for Calculating the Response of Army Vehicles to Blast Waves," Ballistic Research Laboratory Contract Report No. 00369, April 1978, (UNCLASSIFIED). (AD #A056347)

capable of solving three-dimensional problems. The Ballistic Research Laboratory (BRL) wanted to obtain a reliable 3-D hydrocode for shock diffraction loading and free air blast calculations. The two hydrocodes tested in detail are described below.

B. BAAL

One of the several hydrodynamic computer codes being developed at the Los Alamos Scientific Laboratory (LASL) was the implicit, arbitrary-Lagrangian-Eulerian (ALE) hydrocode BAAL⁴. The computing methods used in BAAL are described for two-dimensional flow by Hirt, Amsden, and Cook⁵, and also by Amsden and Hirt⁶. The extension of these methods to three-dimensional flow is described by Pracht⁷. As a result of discussions with representatives of the Ballistic Research Laboratory (BRL), LASL was contracted to perform a computation using the BAAL hydrocode, simulating the three-dimensional shock diffraction loading experiment performed by Taylor¹ at the BRL using a solid rectangular parallelepiped as a target. The results of this computation have been reported⁸. These results have also been reported in the open literature along with a discussion of the solution technique⁹. The BAAL calculation involved a solution of the inviscid Euler equations, with artificial viscosity used to stabilize flow in regions of deceleration. (The BAAL

⁴W. E. Pracht and J. U. Brackbill, "BAAL: A Code for Calculating Three-Dimensional Fluid Flows at All Speeds with an Eulerian-Lagrangian Computing Mesh," Los Alamos Scientific Laboratory Report LA-6342, August 1976.

⁵C. W. Hirt, A. A. Amsden, and J. L. Cook, "An Arbitrary Lagrangian-Eulerian Computing Method for All Flow Speeds," *J. Comp. Phys.* 14, 1974, pp. 227-253.

⁶A. A. Amsden and C. W. Hirt, "YAQUI: An Arbitrary Lagrangian-Eulerian Computer Program for Fluid Flow at All Speeds," Los Alamos Scientific Laboratory Report LA-5100, March 1973.

⁷W. E. Pracht, "Calculating Three-Dimensional Fluid Flows at All Speeds with an Eulerian-Lagrangian Computing Mesh," *J. Comp. Phys.* 17, 1975, pp. 132-159.

⁸R. A. Gentry, L. R. Stein, and C. W. Hirt, "Three-Dimensional Analysis of Shock Loads on a Simple Structure," Ballistic Research Laboratory Contract Report No. 219, March 1975, (UNCLASSIFIED). (AD #B0032081.)

⁹L. R. Stein, R. A. Gentry, and C. W. Hirt, "Computational Simulation of Transient Blast Loading on Three-Dimensional Structures," *Computer Methods in Applied Mechanics and Engineering*, 11, 1977, pp. 57-74.

code has the capability of solving the full Navier-Stokes equations for some flow situations.) In general, the BAAL computation showed excellent agreement with the experimental pressure data for both the front and back faces. Experimental data were not taken on the top and side faces. As a result of the confidence gained in the BAAL code from this comparison, LASL was contracted to perform a second computation. This was for an S-280 Electrical Equipment Shelter struck by a 34.5 kPa (5.0 psi) step shock wave, the reference case discussed earlier. The results of this computation have been reported previously¹⁰. Using the data generated in the BAAL computation¹⁰ for the 34.5 kPa overpressure shock wave diffracting over the shelter, and using a simple scaling model suggested by the BRL to extrapolate the 34.5 kPa data to estimate pressure histories for other comparable shock overpressures, Calligeros et al.¹¹ predicted responses of the shelter to various shock waves for Event Dice Throw. Ethridge¹² has used Taylor's results¹ together with other experimental data to construct correlation functions for blast diffraction loading on the front and rear surfaces of a rectangular parallelepiped. Those correlation functions are compared¹² with the data of Taylor¹ and Lottero¹⁰, showing good agreement.

C. HULL

During approximately the same period that the three-dimensional BAAL computations were being run, a three-dimensional capability was being added to the HULL¹³ hydrodynamic computer code at the US Air Force Weapons Laboratory (AFWL). The major differences between the HULL and BAAL hydrocodes are that HULL solves only the inviscid Euler equations, uses an explicit finite difference algorithm, and is restricted to a fully Eulerian computing mesh comprised of cells which are rectangular parallelepipeds. The AFWL wished to verify the new

¹⁰R. E. Lottero, "Computational Predictions of Shock Diffraction Loading on an S-280 Electrical Equipment Shelter," Ballistic Research Laboratory Memorandum Report No. 2599, March 1976, (UNCLASSIFIED).

¹¹(AD #A022804) J. M. Calligeros, J. P. Walsh, and R. P. Yeghiayan, "Structural Modeling and Response of Command, Control and Communication Shelter Systems for Event Dice Throw," Ballistic Research Laboratory Contract Report No. 00421, March 1980, (UNCLASSIFIED). (AD #A085759)

¹²N. H. Ethridge, "Blast Diffraction Loading on the Front and Rear Surfaces of a Rectangular Parallelepiped," Ballistic Research Laboratory Memorandum Report No. 2784, September 1977, (UNCLASSIFIED).

¹³(AD #A050312) M. A. Fry, R. E. Durret, G. P. Ganong, D. A. Matuska, M. D. Stucker, B. S. Chambers, C. E. Needham, and C. D. Westmoreland, "The HULL Hydrodynamics Computer Code," US Air Force Weapons Laboratory Technical Report 76-183, September 1977, (UNCLASSIFIED).

three-dimensional HULL against existing experimental data or proven codes. The BRL wished to gain access to another reliable three-dimensional hydrocode, because it appeared that BAAL might not be immediately available for production work. The AFWL supplied the computing facilities and the three-dimensional HULL code; the BRL supplied the test problem and the analysis of the hydrocode output.

The problem chosen for the HULL computation was the reference problem described earlier, identical to that run in the second BAAL computation¹⁰ including the flow field grid formulation. This was chosen to gain corroboration for the BAAL computation for the shelter in time for Event Dice Throw.

V. HYDROCODE COMPUTATIONS

Before discussing the results of the hydrocode calculations, the general nature of the computations will be described. This section and its associated Appendix C together describe the direction and index conventions, the computational grid, the computation identifications, various flow parameters, computer mainframes and central processor unit (CPU) times, initial shock locations, and other such characterizing data concerning the computations.

Because the HULL and BAAL codes use different conventions for naming directions and indices, the BAAL results and the flow field diagram are reproduced in part using the HULL hydrocode conventions. Figure 6 shows a 3-D view of the shelter in the computational flow field. The computational grid is discussed in detail in Appendix C.

While there is just one BAAL computation for the shelter, there are two complete HULL computations, designated HULL 19.8063 (hereafter referred to as HULL A) and HULL 19.8067 (hereafter referred to as HULL B). There is also an earlier incomplete HULL computation, designated HULL 202.1 (hereafter referred to as HULL C), that contains some interesting features. All three HULL runs are for the same 34.5 kPa step shock wave. The initial formulations of the four computations are summarized in Table 2.

Analysis by the BRL revealed that the computation for HULL C was not valid after 19 ms simulated problem time because of the arrival of an artificial wave at the front face. The reflected wave from the front face had traveled upstream, eventually arriving at the upstream transmissive boundary through which the HULL code had been feeding the step shock. Because the algorithm for the upstream transmissive boundary was formulated to function as a simple positive image boundary, the initially constant input wave was modified by the arriving compression wave and its following expansion wave. Ultimately, this artificial interaction at the upstream transmission boundary caused the incoming, originally steady, wave to be almost completely turned off, with the artificial wave arriving at the front face by 19 ms simulated problem time.

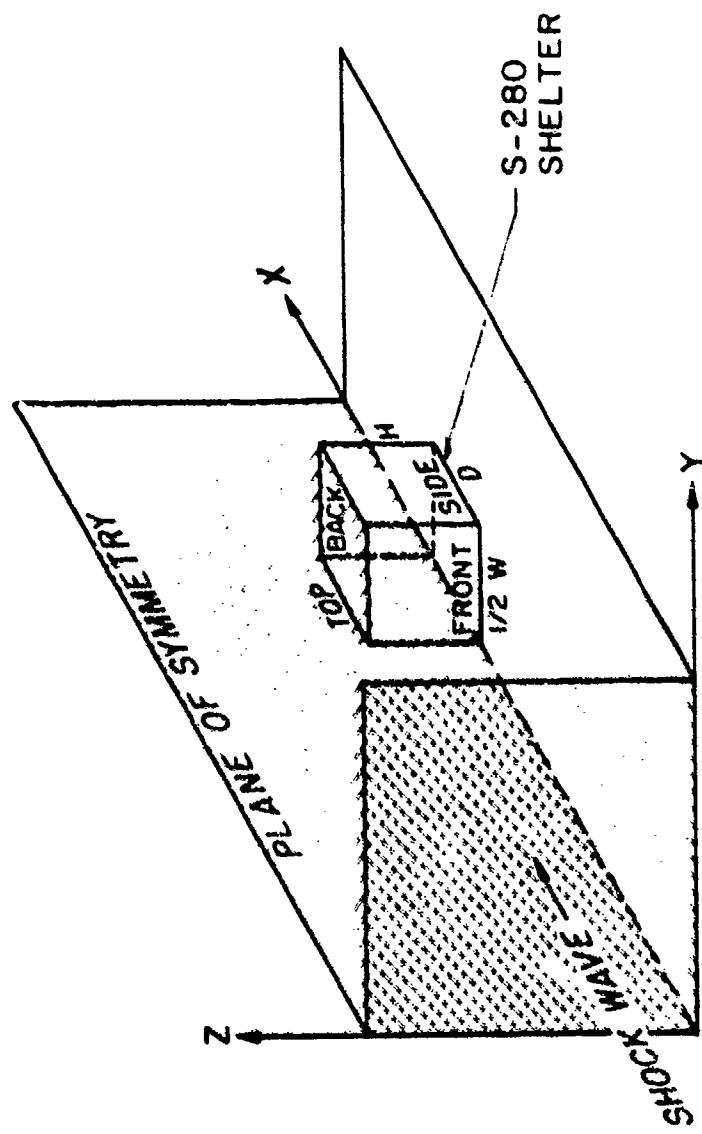


Figure 6. S-280 Electrical Equipment Shelter in the computational flow field.

TABLE 2. HYDRODYNAMIC COMPUTATION SUMMARY, S-2%O SHUTTER, 34.5 kPa (5.0 psi) STEF SHOCK

Computation	Solution of	Grid	Artificial Viscosity	Computer		Comments
				Initial X position of Shock	Time of Courant-Friedrichs-Lowy Number	
BAAL ¹	Euler Equations (Implicit)	Eulerian 8381 cells	Yes	6.2731 m. at front face	≈ 4.0 min (CDC 7600)	Successful run
HULL A	Euler Equations (Explicit)	Eulerian 10602 cells	No	5.3154 m. 7 cells upstream of front face	20.5 min (CDC 6600) CFL = .50	Successful run
HULL B	Euler Equations (Explicit)	Eulerian 10602 cells	No	6.2731 m. at front face	18.2 min (CDC 6600) CFL = .50	Successful run
HULL C	Euler Equations (Explicit)	Eulerian 10602 cells	Yes	6.2731 m. at front face	time not available CFL = .15	Early HULL run, Artificial waves reached front face after 19 ms simulated problem time

With the information from the analysis of HULL C and from extensive analyses of other problems by AFWL, improvements to 3-D HULL were made by AFWL. The problems labeled HULL A and HULL B were run at AFWL in a cooperative effort by the BRL and AFWL using the improved 3-D HULL. These two HULL runs are identical except that for HULL A the shock is started at seven flow field cells upstream of the S-280 shelter front face, whereas for HULL B the shock is started at the front face of the shelter, as was the case for the BAAL run and HULL C. Artificial viscosity was used for both the BAAL run and HULL C; no artificial viscosity was used in HULL A or HULL B. Also, HULL C was run with a Courant-Friedrichs-Lowy (CFL) stability factor $\eta = 0.15$, while both HULL A and HULL B used $\eta = 0.50$.

VI. LOADING ON SHELTER FACES

A. Remarks

This section contains detailed discussions of the loading on the shelter, with individual sections on the front, back, top, and side faces. The hydrocode results and the predictions made from the Technical Manual's and Taylor's semiempirical models are compared with one another.

B. Front Face

Figure 7 shows a comparison of the average overpressure on the front face of the shelter computed with BAAL; HULL runs A, B, and C; the Technical Manual; and Taylor's model. The two simple models both show the theoretical peak overpressure of 78.5 kPa at time zero. The first data point for the BAAL computation is at $t = 1.57$ ms, showing an average overpressure of 74.3 kPa for the front face, 5.4 percent below the theoretical peak value. No pressure data prior to this time were furnished to the BRL, and hence the character of the BAAL computation from $0 \leq t < 1.57$ ms is unknown.

HULL C is the HULL computation that most closely resembles the BAAL computation in its general nature. These two computations use essentially the same grid (See Appendix C); they are both started with the shock at the front face. Both computations use a form of artificial viscosity, applying it only in regions of deceleration, although the actual form of the BAAL viscosity function¹⁴ is different from that used in the HULL code¹⁴. As can be seen in Figure 7, the HULL C computation appears to be stable from time zero up to 19 ms, after which the

¹⁴P. W. Lunn, H. J. Happ III, and C. E. Needham, "Development of an Artificial Viscosity Function," US Air Force Weapons Laboratory Technical Report 77-53, September 1977, (UNCLASSIFIED).

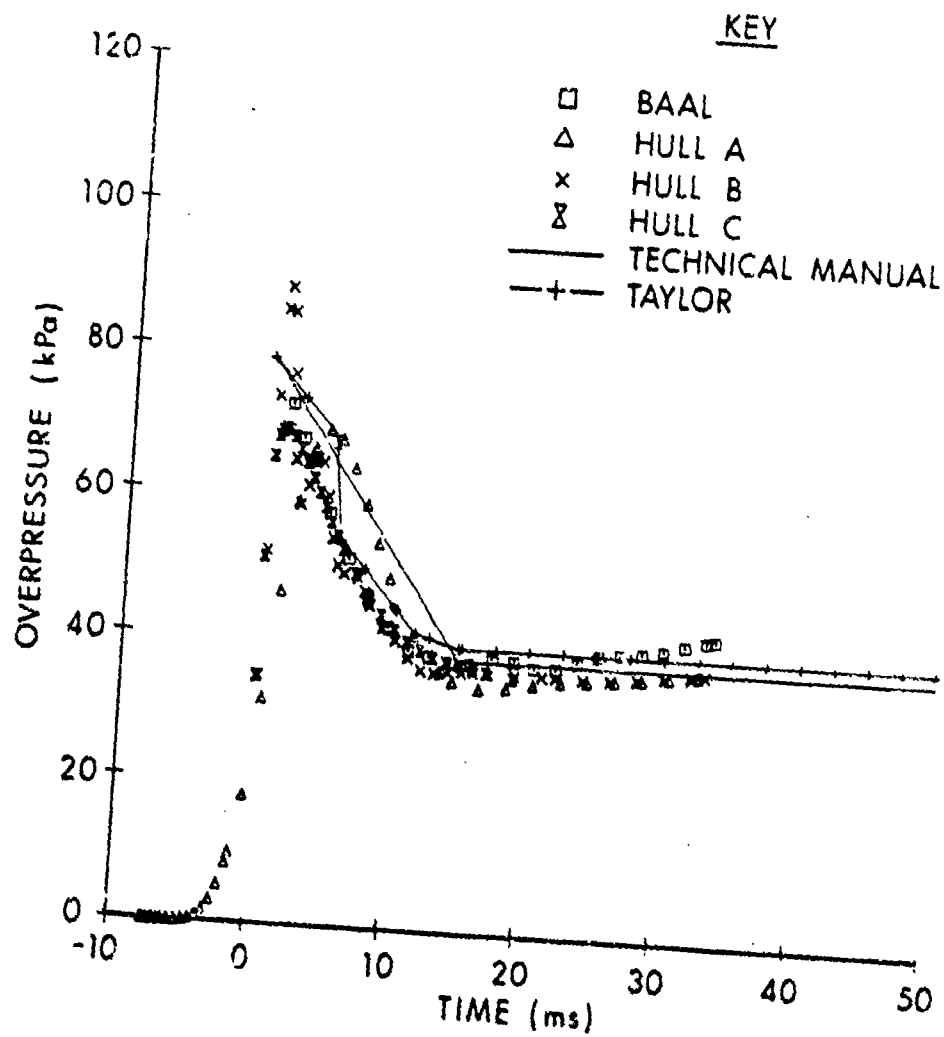


Figure 7. Front face average overpressure.

solution drops off significantly due to the arrival of the artificial wave discussed earlier. The computation after 19 ms is not plotted. The HULL C computation reaches a peak average overpressure of approximately 69.0 kPa at 1.3 ms, 12.1 percent less than the theoretical peak. From a time of 2.5 ms to 17 ms, the BAAL and HULL C computations are nearly identical. After this time, the BAAL computation tends to rise to values above the others, whereas the HULL C computation begins to converge with the other HULL computations until it is destroyed by the artificial wave.

The agreement between the HULL C and BAAL runs is quite remarkable, particularly so because the HULL code is using a computational grid designed for BAAL. Normally, the HULL code uses grids in which the cell-to-cell variation in size is kept to less than 5 to 10 percent in the region where the solution is desired, or in any region through which a wave must pass on its way to the region where the solution is desired. The BAAL grid has cell-to-cell variations in size on the shelter face of 25 percent in the X direction, and as large as 25 percent for most cells in the Y and Z directions, with much larger variations in the general flow field away from the shelter. As indicated in earlier work¹⁰ there is excellent agreement between the experimentally measured average overpressure and the average overpressure computed with BAAL for the front face of a rectangular parallelepiped, using a similar grid. This agreement gives reason for confidence in the validity of the BAAL computation for the shelter front face, except for late time where the average overpressure computed with BAAL seems high, and for pressure anomalies in the computation at the edges of the front face.

The next comparison of interest in Figure 7 is that of HULL C with HULL B. The input data, initial flow fields, and finite difference grids for these two computations are identical except that HULL B uses $n = 0.50$ and no artificial viscosity, and HULL C uses $n = 0.15$ with artificial viscosity turned on. There are significant differences between the results of the two computations early in the diffraction phase. The HULL B computation shows an overshoot of the average overpressure to a peak value of 88.5 kPa at 1.0 ms, 12.7 percent above the peak theoretical value of 78.5 kPa, and 28.2 percent above the peak average overpressure of 69.0 kPa at 1.3 ms in the HULL C computation. The HULL B computation also shows significant oscillation about the results of the HULL C computation for $t \leq 6$ ms. It is doubtful that the higher CFL number, n , for HULL B is the primary cause of this oscillation; it is more likely due to running the code without artificial viscosity, combined with having the shock started as a discontinuity at the shelter front face. It is of interest to note that at 1.6 ms (the HULL B datum closest in time to the first datum of the BAAL computation at 1.571 ms) the HULL B computation shows an average overpressure of 76.4 kPa, 2.7 percent less than the theoretical peak reflected overpressure of 78.5 kPa.

The setup of the HULL A computation is identical with that of the HULL B computation except that the HULL A computation begins with the shock located seven flow field cells upstream of the shelter front face. As can be seen in Figure 7, the movement of the shock through those seven flow field cells results in a significantly different average overpressure history on the shelter front face for HULL A compared with HULL B. Signals from the computational shock in HULL A, spatially in the form of a forward, exponentially decreasing function, arrive well ahead of the theoretical shock arrival time. These early signals are then reflected back continuously into the main portion of the on-coming computational shock wave, ultimately reducing the peak over-pressure, and delaying and spreading it in time. The peak average overpressure for HULL A is 69.0 kPa, 12.1 percent less than the theoretical peak, occurring at 4.35 ms after the theoretical arrival time of the shock wave at the front face. By 4.35 ms, the theoretical location of the shock wave is actually 1.68 m downstream of the front face, 77.5 percent of the distance to the plane of the back face. Gentry et al.⁸ show the same qualitative effect in comparing the results of a BAAL computation for a step shock started at the front face of a rectangular parallelepiped with that for an identical shock in the same grid started five flow field cells upstream of the front face.

The almost exact agreement in peak average overpressure for the shelter front face between HULL C and A is most likely coincidental. The effect manifesting itself in HULL A is numerical diffusion caused by using a CFL number less than 1.0 ($n = 0.50$) and having the shock move through seven highly nonuniform flow field cells prior to interacting with the shelter. The X-direction cell-to-cell variation in size between the seventh and sixth cells upstream of the shelter front face is 45.0 percent. The early time effects in HULL C governing the development of the peak average overpressure on the front face are due almost entirely to the effects of the modifications via artificial viscosity to the pressure difference^{14,15} used to compute the accelerations in the Lagrangian phase of the HULL computation¹³. The HULL A and HULL B computations converge with one another by 20 ms, as should be expected. The HULL C computation appears to have been tending toward converging with the other HULL computations just prior to its being destroyed by the artificial wave discussed earlier.

The solutions obtained by using the model outlined in the Technical Manual and that suggested by Taylor¹ are also shown in Figure 7. All six average overpressure histories suggest that the wave interaction, or diffraction, phase on the front face lasts for about 15 ms, and is then followed by the drag phase. The Technical Manual solution for the diffraction phase is significantly different

¹⁵R. D. Richtmyer and K. W. Morton, "Difference Methods for Initial Value Problems," 2d Ed., Interscience Publishers, Inc., New York, New York, 1967, pp. 311-317.

from all of the other solutions, except that it is nearly identical to Taylor's solution in the early part of the diffraction phase. It agrees well with the HULL B solution throughout the drag phase, with the BAAL and HULL C solutions in the early drag phase, and with the HULL A solution shortly after the beginning of the drag phase. The overpressure calculated with Taylor's model, although it is somewhat high, shows good agreement with the hydrocode solutions throughout the diffraction phase, except for regions where the hydrocode solutions show the questionable behavior discussed earlier. This good agreement, coupled with the ease with which the model may be applied, makes Taylor's model most attractive for estimating front face diffraction loading. Taylor's solution for the drag phase is consistently above all of the others, except for the late-time BAAL solution.

Appendix D contains a comparison of the HULL B prediction for average overpressure on the shelter front face with Ethridge's¹² empirical correlation function and a gage weighting function used by Taylor¹.

C. Back Face

Figure 8 shows a comparison of the average overpressure on the back face of the S-280 shelter as computed by BAAL, HULL runs A and B, the Technical Manual, Taylor's¹ suggested improvement to the Technical Manual model, and a proposed model. There is excellent agreement among the three hydrocode computations. The results for the two existing semiempirical models^{1,2} differ from those for the hydrocodes, particularly the model from the Technical Manual. As indicated by Gentry et al.⁸, the average overpressure on the back face in the BAAL computation for the rectangular parallelepiped agrees quite well with the experimentally measured average overpressure. This led to the conclusion that the average overpressure on the back face of the shelter as computed with BAAL may also be considered to be an accurate estimate. This conclusion is strongly reinforced by the agreement shown by HULL runs A and B. The three hydrocode computations show a much faster rise time required to reach the peak average overpressure, and that the peak is higher than that predicted by the semiempirical models. The hydrocodes also indicate a local pressure peak around 19 ms, most likely due to the interaction with one another of the weakened shocks breaking over the top and around the side faces.

It is a fairly direct matter to modify the existing models for average overpressure on the back face to better fit the hydrocode results, at least for this case. As before, Equation (3) gives $t_d = 5.62$ ms, with $\bar{p}_b^* = 0.0$ for $t \leq t_d$. It is proposed that the constant a in Equation (4) be modified so that $a = 2$. The modified rise time is then $(t_b)_{rise} = 10.64$ ms. The peak average overpressure on the back face may be computed by using a modified version of Equation (5).

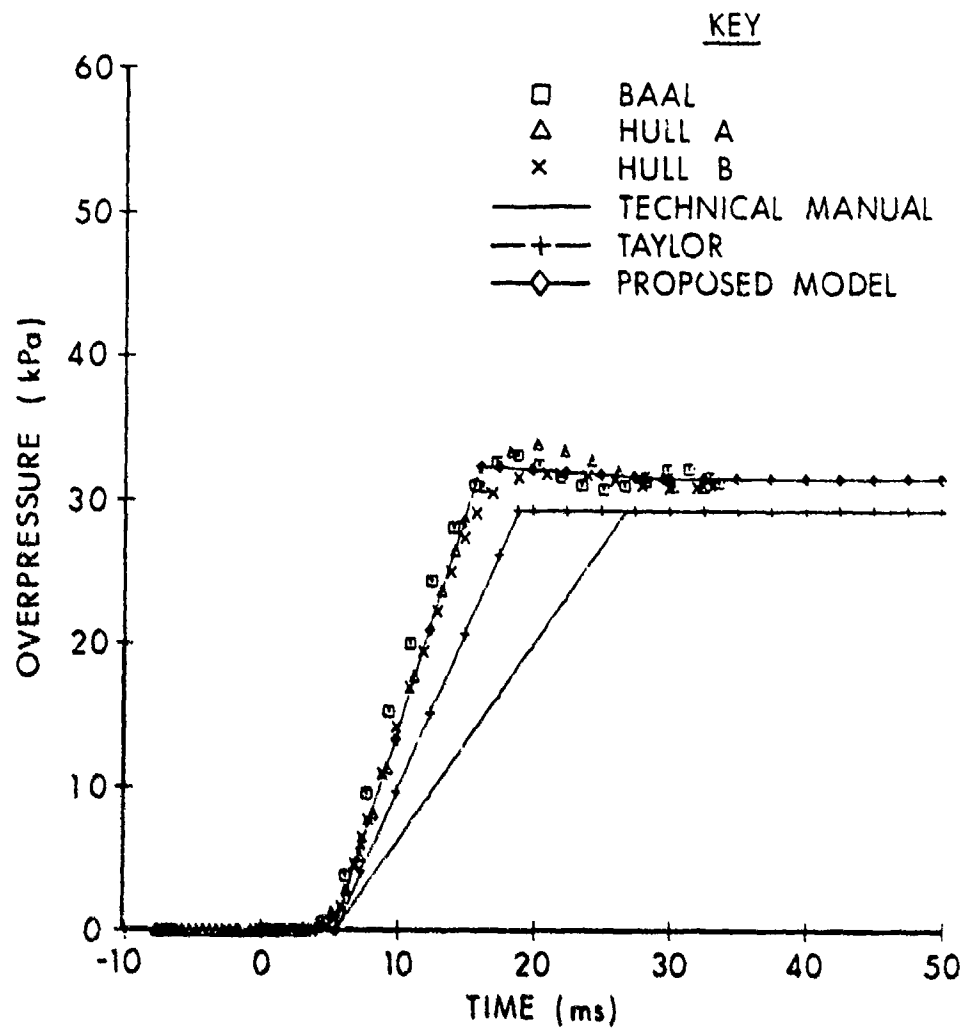


Figure 8. Back face average overpressure.

$$(\bar{p}_b^*)_{\max} = p^*(t)_b \left(\frac{1}{2} \right) \left[1 + (1-\beta)e^{-n\beta} \right], \quad (12)$$

with $n = -\frac{1}{3}$ and $p^*(t)_b = (p_2 - p_1)$. The average overpressure on the back face, \bar{p}_b^* , varies linearly from a value of 0.0 at $t = t_d$ to $(\bar{p}_b^*)_{\max}$ at $t = t_d + (t_b)_{\text{rise}}$. For the present case, $(\bar{p}_b^*)_{\max} = 32.4 \text{ kPa}$ at $t = 16.3 \text{ ms}$.

There is a decompression phase, lasting from

$$\left[t_d + (t_b)_{\text{rise}} \right] \leq t \leq \left[t_d + (t_b)_{\text{rise}} + \frac{(2.5)h}{c_1} \right], \quad (13)$$

where (\bar{p}_b^*) varies linearly from $(\bar{p}_b^*)_{\max}$ to the value $(\bar{p}_b^*)_{\text{drag}}$. This value is found by substituting $n = 0$ into Equation (12), so that

$$(\bar{p}_b^*)_{\text{drag}} = p^*(t)_b \left(\frac{1}{2} \right) (2-\beta). \quad (14)$$

Equation (14) gives the average overpressure on the back face for a step shock for all $t \geq \left[t_d + (t_b)_{\text{rise}} + \frac{2.5h}{c_1} \right]$. For the present case, $(\bar{p}_b^*)_{\text{drag}} = 31.5 \text{ kPa}$ for $t \geq 29.6 \text{ ms}$. This modified model is shown in Figure 8. It fits the hydrocode data well, but its generality, like that of the model on which it is based, may be questionable.

D. Top Face

Figure 4 shows the average overpressure on the top face of the shelter as computed by BAAL, HULL runs A and B, the Technical Manual, and a proposed model. There is excellent agreement between the BAAL and HULL B computations throughout the range of simulated time. The HULL A computation agrees quite well with the other two hydrocode computations for $0 \leq t \leq 7 \text{ ms}$, and for $t \geq 16 \text{ ms}$. For $7 \leq t \leq 16 \text{ ms}$, the HULL A solution shows a higher, more delayed peak compared with the other computations. This is most likely caused by the delayed, extended, and less strong reflection that the HULL A computation shows for the front face. The HULL A computation also shows some top face loading for $t < 0 \text{ ms}$, indicating the arrival of the forward portion of the computational shock ahead of the theoretical shock arrival time.

The solid line in Figure 4 represents the average overpressure for the top face as computed by using the model suggested in the Technical Manual. The agreement with the hydrocodes for the first 6 ms, approximately equal to the time required for the theoretical shock wave to

travel along the top face, is excellent. However, the model under-predicts the peak average overpressure computed by the hydrocodes, and shows poor agreement for $t > 6$ ms. As with the models for the back face, the Technical Manual model for the top and side faces can be modified without much difficulty to give excellent agreement with the hydrocode results.

The following modified version of Equation (7) is proposed for computing the average overpressure on the top face,

$$(\bar{p}_{\text{top}}^*) = (p_2 - p_1) \left[A + (1 - A) \left(1.0 - \frac{p_2 - p_1}{p_1} \right)^2 \right]. \quad (15)$$

where A is a constant whose value depends on whether the maximum, local minimum, or drag phase overpressure is to be computed. After a delay time t_d as defined in Equation (3), the maximum average overpressure on the top face, $(\bar{p}_{\text{top}}^*)_{\text{max}}$, is computed by setting $A = 1$, so that Equation (15) reduces to

$$(\bar{p}_{\text{top}}^*)_{\text{max}} = (p_2 - p_1). \quad (16)$$

From time $t = 0$ to $t = t_d$, the average overpressure increases linearly from zero to $(\bar{p}_{\text{top}}^*)_{\text{max}}$. From time $t = t_d$ to a time

$$(t_{\text{top}})_{\text{pmin}} = t_d + \frac{2.0 D}{W_i}, \quad (17)$$

the average overpressure on the top face decreases linearly from $(\bar{p}_{\text{top}}^*)_{\text{max}}$ to a value $(\bar{p}_{\text{top}}^*)_{\text{pmin}}$, which is computed by setting $A = 0.6$ in Equation (15). From time $(t_{\text{top}})_{\text{pmin}}$ to a time

$$(t_{\text{top}})_{\text{drag}} = (t_{\text{top}})_{\text{pmin}} + \frac{1.5 D}{W_i}, \quad (18)$$

the average overpressure on the top face increases linearly from $(\bar{p}_{\text{top}}^*)_{\text{pmin}}$ to a value $(\bar{p}_{\text{top}}^*)_{\text{drag}}$, which is computed by setting $A = 0.8$ in Equation (15); after this time the average overpressure remains at $(\bar{p}_{\text{top}}^*)_{\text{drag}}$. Thus, instead of dealing with several different equations as suggested in the Technical Manual², it is only necessary to deal with an equation of the form of Equation (15), with $A = 1.0$ for the maximum, $A = 0.6$ for the minimum, and $A = 0.8$ for the drag phase average overpressures. For the present case, the model proposed

above predicts $\bar{p}_{top}^* = 0.0$ kPa at $t = 0.0$ s, $(\bar{p}_{top}^*)_{max} = 34.5$ kPa at $t_d = 5.62$ ms, $(\bar{p}_{top}^*)_{pmin} = 26.7$ kPa at $(t_{top}^*)_{pmin} = 16.8$ ms, and $(\bar{p}_{top}^*)_{drag} = 30.6$ kPa for $t \geq (t_{top}^*)_{drag} = 25.3$ ms. The history of average overpressure for the top face as predicted by the modified model proposed above is shown in Figure 4.

E. Side Face

Figure 5 shows the average overpressure on the side face of the shelter as computed by BAAL, HULL runs A and B, the Technical Manual, and the proposed model. The proposed model, a modification of the Technical Manual model, is also to be used for both the top and side faces of the shelter. Because of the geometry of the shelter, the side face is nearly equivalent in size to the half of the top face that is actually simulated in the hydrocode solutions (the top face is cut in half by a symmetry plane), and because they have similar orientations in the flow field, the hydrocode solutions for the side face are nearly identical with those for the top face. Therefore, the same comments regarding the relative performance of the hydrocodes and the existing models for the top face loading also apply to the side face loading. As noted for the modified model proposed for the back face loading, the generality of this proposed modified model may also be limited.

VII. NET LOADING

A. Definition

An important point stressed by Taylor¹ is that the method outlined in the Technical Manual significantly overestimates the net loading on a 3-D target, with net loading defined as the average overpressure on the front face minus that on the back face. Taylor's model predicts a lower net load on the shelter than does the Technical Manual model.

B. Discussion

It is appropriate at this time to refer back to the BAAL and HULL B plots of overpressure versus time in Figure 2 and the net loading plots shown in Figure 3. There are several reasons why only the BAAL and HULL B computations are chosen for comparison. The HULL C solution for the front face is valid only up to 19 ms, as discussed earlier; the solution for the back face is no longer available, but in view of the problems associated with this computation, it would probably be of limited value. The HULL A solution shows significant deviation from the other hydrocode solutions, most likely due to the diffusion of the computational shock after its having been started seven cells upstream of the shelter front face. Both the BAAL and HULL B solutions start with the computational shock at the front face.

As shown in Figure 2, except for the BAAL computation later in the drag phase ($t > 20$ ms) and the HULL B computation near $t = 0$, both hydrocode solutions are consistently below the front face average overpressure predicted by either Taylor's model or the Technical Manual model. Conversely, both hydrocode solutions for the back face indicate that the back face is loaded even more rapidly than Taylor suggests, peaking and remaining at average overpressure values well above those predicted by either of the two models for all of the time represented here. Viewed together, the front and back face loadings from the hydrocode solutions show a greatly reduced net load on the shelter, as may be seen in Figure 3. The curves in Figure 3 suggest that the diffraction phase for the entire shelter is essentially over by 20 to 25 ms, or approximately four crossing times. During the diffraction phase, both hydrocode solutions show much less net loading than that predicted by Taylor¹, which is in turn much less than that predicted by using the model in the Technical Manual. The implication is that the whole body response of a 3-D target during the diffraction phase (which can be relatively long compared with a single crossing time based on the depth of the structure) may be significantly less than the simple models predict.

By 25 ms, the net loadings from each of the two hydrocode solutions shown in Figure 3 have begun to diverge from one another. The net loading from the HULL B solution increases with time, but remains less than that for both of the semiempirical model solutions. The BAAL solution eventually becomes greater than all of the others; this may be an artifact of the BAAL computation, but that is yet to be determined. The data in Figure 3 suggest that the drag phase for the structure as a whole begins at 20 to 25 ms.

Structural damage to the shelter is generally done during the diffraction phase: the walls are driven inward and can damage the equipment inside, reducing or ending its usefulness. At assumed threat levels, the diffraction phase produces relatively little whole-body motion of the shelter; this motion can occur in the drag phase. It may be that the shelter and the equipment inside will survive the diffraction phase but will be destroyed by having the shelter roll over and impact the ground in the drag phase. Thus, understanding what the shelter loading is during the drag phase is essential. Yet it is during the drag phase that the limited computational and semiempirical data that are available (such as are shown in Figure 3) disagree. Additional experimental and computational data in the drag phase for three-dimensional structures are needed to better quantify the loading during this phase.

VIII. ROTATIONAL MOMENT

Neither the existing semiempirical models nor the proposed model provide any information concerning the locations of the centers-of-overpressure on the surfaces of a target as a function of time; wave interaction models could provide such estimates. The TRUCK code³, which discretizes surfaces for its wave interaction computations, does provide this capability. To the extent of the credibility of the hydrocodes and the solutions gained by their use, such information is readily available¹⁰.

Figure 9 shows the history of the Z location of the center-of-overpressure for the front face of the shelter as computed by BAAL, and by HULL runs A and B. The three hydrocode solutions show remarkable agreement with one another, although the slight differences do seem to be systematic. The center-of-overpressure stays quite close to half way up the front face for nearly all of the simulated time, except for a slight movement downward during the early part of the diffraction phase.

Figure 10 shows the history of the Z location of the center-of-overpressure for the back face of the shelter as computed by the same three hydrocode runs. The back face shows considerable variation in the location of the center-of-overpressure during the diffraction phase. Prior to the arrival of the shock wave, the center-of-overpressure is arbitrarily defined as being at one-half of the height of the shelter; during that time, the average overpressure is zero by definition. The HULL A plot indicates the arrival of the forward section of the computational shock prior to the theoretical arrival time of $t = 5.62$ ms at the plane of the back face.

The center-of-overpressure histories on the shelter front and back faces take on added significance when considered in conjunction with the average overpressure histories on the respective faces, just as the average loadings on the front and back faces do when looked at together in Figures 2 and 3. The semiempirical models^{1,2} predict higher loading on the front face than do the hydrocodes. For lack of a better estimate, it might seem reasonable to use the centroid of the target face for the location of the center-of-overpressure on both the front and back faces when using the semiempirical models. The hydrocodes indicate that such an approximation would be reasonable for the front face, but not so for the diffraction phase on the back face.

During the early part of the diffraction phase, the hydrocodes predict a significantly greater average overpressure on the back face than do the semiempirical models, acting considerably above the mid-point on the back face. During the remainder of the time simulated by the hydrocodes, the computed loading is still well above that predicted by the semiempirical models, but with the center-of-overpressure near the area centroid. Specifically, an average of the BAAL and HULL B

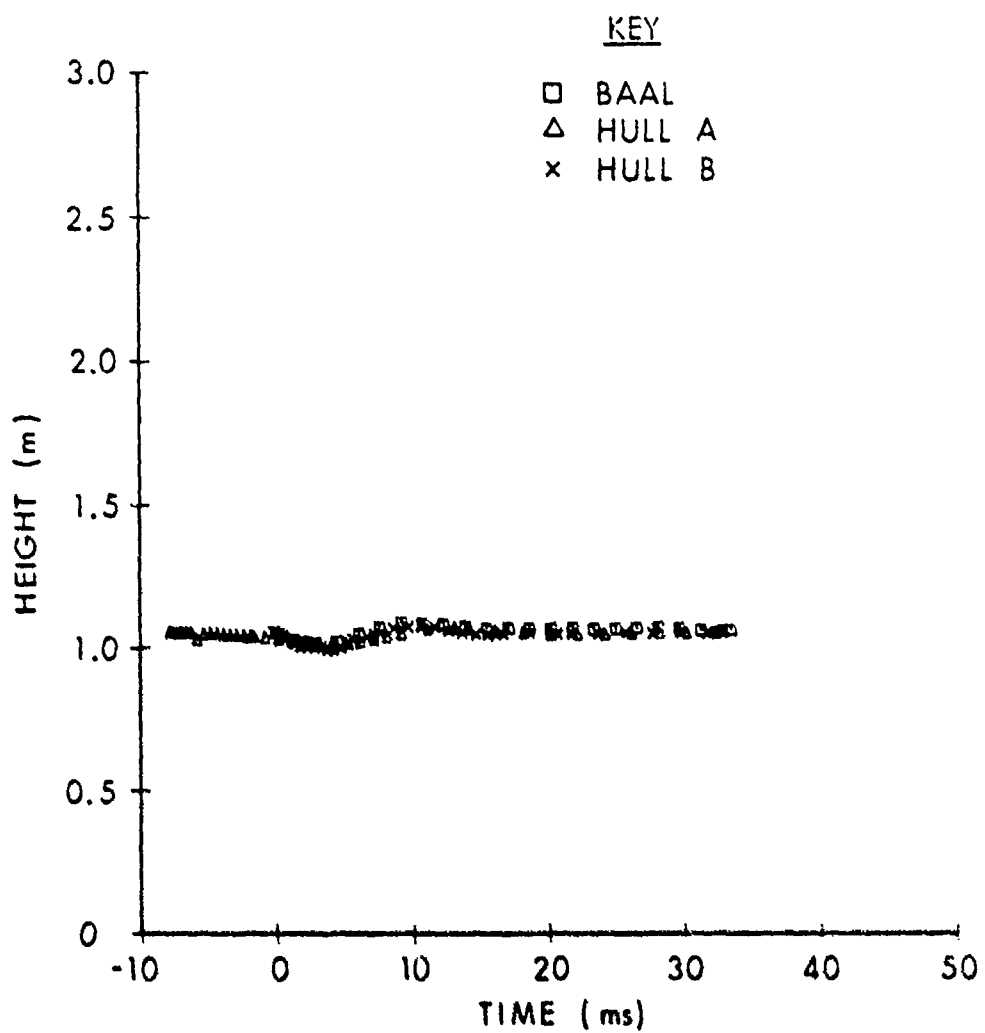


Figure 9. Height of center-of-overpressure on front face.

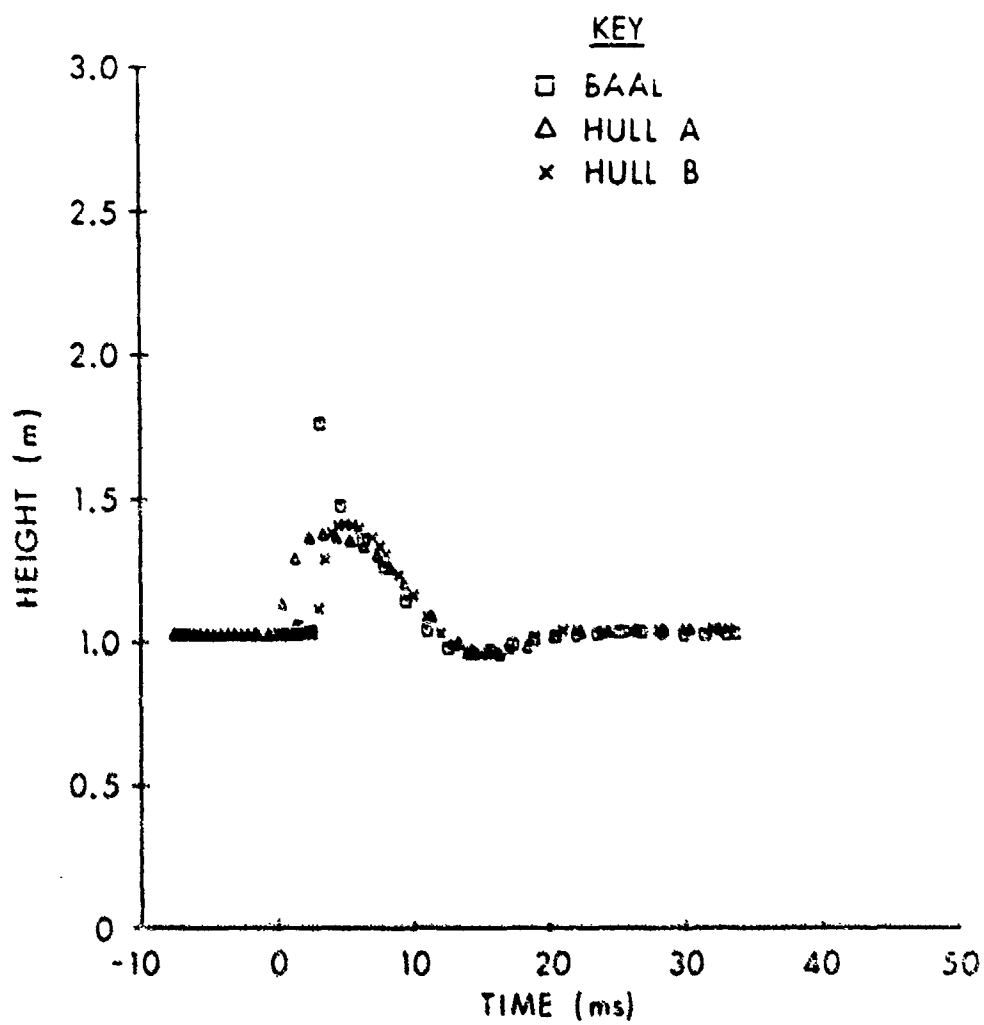


Figure 10. Height of center-of-overpressure on back face.

average overpressure on the back face over the time interval $6.6 \leq t \leq 15.8$ ms is 151 percent greater than that predicted by the Technical Manual, and 57 percent greater than that predicted by Taylor's model. For the time interval $17.2 \leq t \leq 33.4$ ms, the two hydrocode solutions average 30 percent greater than the Technical Manual and 8.7 percent greater than Taylor's model.

The histories of the net rotational moment due to overpressure on the shelter computed by using BAAL, HULL B, and each of the two semi-empirical models are shown in Figure 11. The rotational moments are computed about a line in the plane of the bottom boundary and perpendicular to the side face. As was the case for the net loading curves in Figure 3, Taylor's model¹ yields rotational moments larger than those for the Technical Manual very early in the diffraction phase and also in the drag phase, but significantly smaller values throughout the majority of the diffraction phase. The HULL B computation shows the oscillation in the solutions in the early diffraction phase as discussed earlier. For $4 \leq t \leq 20$ ms the HULL B and BAAL solutions show excellent agreement with one another, predicting values well below those for the simple models. During that time interval, the hydrocodes average 47 percent less than that predicted by the Technical Manual, and 31 percent less than that predicted by Taylor's model. For $t > 20$ ms, the BAAL and HULL B solutions diverge significantly from one another. By 33.1 ms, the HULL B computation has reached a net rotational moment due to overpressure of 55.0 kN-m, 20.3 percent less than the Technical Manual model's value of 69.0 kN-m, and 33.5 percent less than the value of 82.7 kN-m obtained by using Taylor's model. By 33.6 ms, the BAAL computation has reached a net rotational moment due to overpressure of 97.8 kN-m, 41.7 percent greater than the value from the Technical Manual model, 19.3 percent greater than the value from Taylor's model, and 77.8 percent greater than the value from the HULL B computation at 33.1 ms.

The reason for this divergence is two-fold. The BAAL computation shows much higher late-time overpressure on the front face of the shelter than does the HULL B computation, as shown in Figure 7, with a center-of-overpressure consistently above that for the HULL B computation, as shown in Figure 9. Conversely, the BAAL computation shows only somewhat higher late-time overpressure on the back face of the shelter than does the HULL B computation, as shown in Figure 8; it has a center-of-overpressure consistently below that for the HULL B computation, as shown in Figure 10. At least part of the reason for this difference in behavior between the two hydrocode solutions is the apparent anomalous behavior in the BAAL solution discussed earlier.¹ More information on the grid and the anomalous behavior is presented in Appendices C and E.

If the hydrocode computations are correct, as they appear to be, then the net rotational moment on a 3-D structure may be much less than would be indicated by the existing semiempirical models. This indicates less vulnerability to overturning than may have previously been assumed.

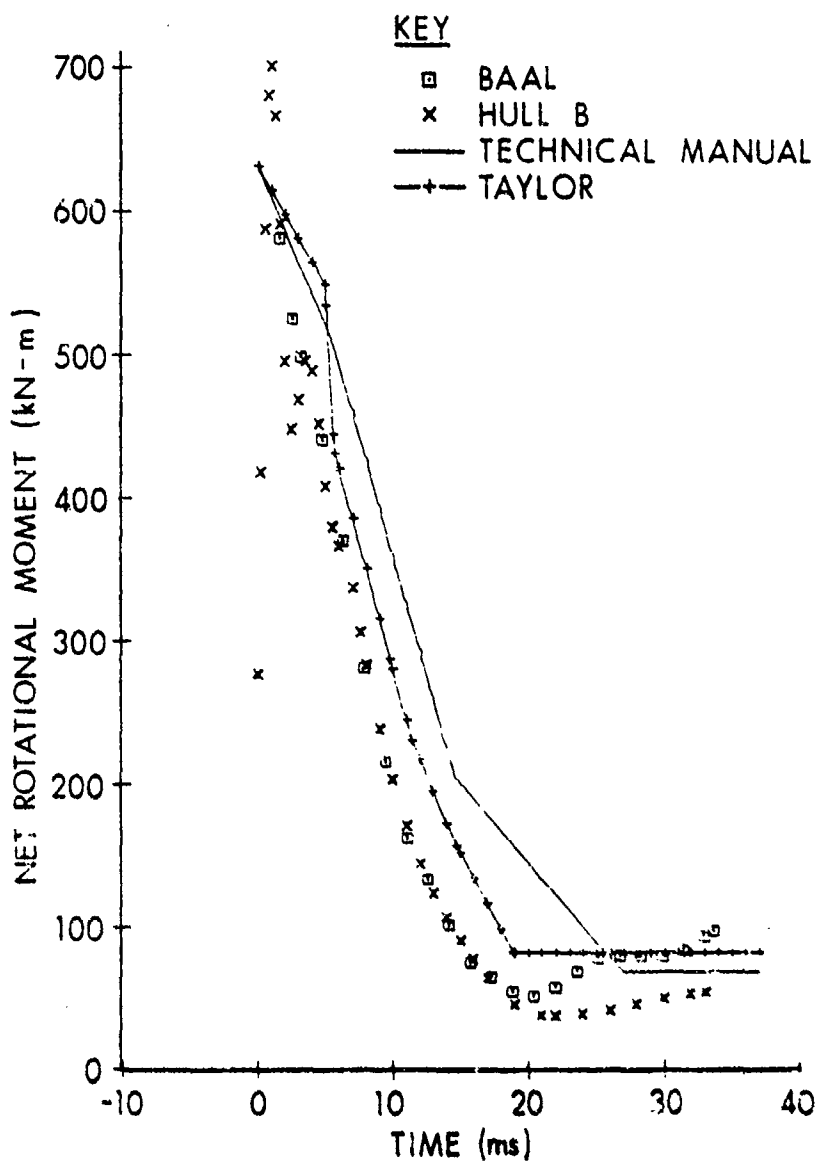


Figure 11. Net rotational moment due to overpressure.

IX. CONCLUSION

In general, the hydrocodes show good agreement with one another in predicting overpressure averaged over each of the given faces of the S-280 Electrical Equipment Shelter. They are also useful as comparative tools in evaluating the capability of the semiempirical models to predict such loading. Additionally, the hydrocodes provide a great deal of information for which more easily used predictive models (similar to the semiempirical models discussed here) are not available and which is not readily gathered experimentally. An example of this is the use of the data from the hydrocodes to make accurate estimates of the location vs time of the center-of-overpressure for use in computing rotational moments. Also, the analysis of the various hydrocode results discussed here has allowed some quantification of the effects of such items as the value of the CFL number, numerical diffusion caused by the finite difference grid, and artificial viscosity.

The model outlined in the Technical Manual does not appear to be suitable for predicting either the shock diffraction or the drag phase loading on a three-dimensional structure such as the S-280 Electrical Equipment Shelter. The front face loading prediction for the diffraction phase seems to be too high; the prediction for the drag phase appears to be reasonable. The prediction for the back face loading is too low, and is made worse by predicting too long a rise time for overpressure to go from zero to the predicted drag phase value. The models for predicting the loading on the top and side faces are fairly good at predicting the initial increase of average overpressure with time, but they underestimate its peak value; thereafter, the models appear to be significantly in error.

Taylor's model¹ for estimating the average overpressure on the front of a three-dimensional structure is a significant improvement over the model suggested in the Technical Manual, particularly during the diffraction phase. However, predictions of average overpressure in the drag phase using Taylor's model appear to be somewhat high compared with the hydrocode predictions. The change suggested by Taylor to the Technical Manual model for the average overpressure on the back face is an improvement, but it too underpredicts the loading for all time, missing the peak overpressure and overestimating the time required to reach the predicted peak overpressure. Taylor did not address the top and side face loading.

The empirical models suggested by Ettridge¹² provide a quick and fairly accurate means of estimating the average overpressure as a function of time on both the front and back faces of a rectangular parallelepiped. The modifications to the models in the Technical Manual for the back, top, and side faces of a rectangular parallelepiped proposed in this report also provide a quick, accurate means of estimating average overpressure, with the added feature of providing some of the detailed loading variations observed in the hydrocode computations.

The semiempirical models do not provide a means for computing the time-history of the center-of-overpressure on the various faces of the structure. As a result, it is not possible to compute rotational moments unless assumptions are made concerning the location of the center-of-overpressure. Alternatively, center-of-overpressure models could be developed. The hydrocodes do provide this information.

The hydrocodes and the semiempirical models all provide conflicting information during the drag phase. This late-time loading is important because it is during this time that overturning either will or will not take place. Unfortunately, relatively little experimental data have been gathered for late-time loading. This problem needs to be resolved both experimentally and computationally. Comparison of late-time loading obtained via experiment with that from inviscid codes such as HULL will also be of value in determining whether or not viscous effects should be modeled.

REFERENCES

1. W. J. Taylor, "A Method for Predicting Blast Loads During the Diffraction Phase," The Shock and Vibration Bulletin, NR. 42, Part 4 of 5, Shock and Vibration Center, Naval Research Laboratory, Washington, DC, p. 135 (Jan 72).
2. "Design of Structures to Resist the Effects of Atomic Weapons," US Army Corps of Engineers EM-1110-445-413, 1 July 1959, (UNCLASSIFIED). (Republished as TM5-856-1 in 1965.)
3. N. P. Hobbs, J. P. Walsh, G. Zartarian, W. N. Lee, and Y. Wu, "TRUCK - A Digital Computer Program for Calculating the Response of Army Vehicles to Blast Waves," Ballistic Research Laboratory Contract Report No. 00369, April 1978, (UNCLASSIFIED). (AD #A056347)
4. W. E. Pracht and J. U. Brackbill, "BAAL: A Code for Calculating Three-Dimensional Fluid Flows at All Speeds with an Eulerian-Lagrangian Computing Mesh," Los Alamos Scientific Laboratory Report LA-6342, August 1976.
5. C. W. Hirt, A. A. Amsden, and J. L. Cook, "An Arbitrary Lagrangian-Eulerian Computing Method for All Flow Speeds," J. Comp. Phys. 14, 1974, pp. 227-253.
6. A. A. Amsden and C. W. Hirt, "YAQUI: An Arbitrary Lagrangian-Eulerian Computer Program for Fluid Flow of All Speeds," Los Alamos Scientific Laboratory Report LA-5100, March 1973.
7. W. E. Pracht, "Calculating Three-Dimensional Fluid Flows at All Speeds with an Eulerian-Lagrangian Computing Mesh," J. Comp Phys. 17, 1975, pp. 132-159.
8. R. A. Gentry, L. R. Stein, and C. W. Hirt, "Three-Dimensional Analysis of Shock Loads on a Simple Structure," Ballistic Research Laboratory Contract Report No. 219, March 1975, (UNCLASSIFIED). (AD #B003208L)
9. L. R. Stein, R. A. Gentry, and C. W. Hirt, "Computational Simulation of Transient Blast Loading on Three-Dimensional Structures," Computer Methods in Applied Mechanics and Engineering 11, 1977, pp. 57-74.
10. R. E. Lottero, "Computational Predictions of Shock Diffraction Loading on an S-280 Electrical Equipment Shelter," Ballistic Research Laboratory Memorandum Report No. 2599, March 1976, (UNCLASSIFIED). (AD #A022804)

REFERENCES (Continued)

11. J. M. Calligeros, J. P. Walsh, and R. P. Yeghiyan, "Structural Modeling and Response of Command, Control and Communication Shelter Systems for Event Dice Throw," Ballistic Research Laboratory Contract Report No. 00421, March 1980, (UNCLASSIFIED). (AD #A085759)
12. N. H. Ethridge, "Blast Diffraction Loading on the Front and Rear Surfaces of a Rectangular Parallelepiped," Ballistic Research Laboratory Memorandum Report No. 2784, September 1977, (UNCLASSIFIED). (AD #A050312)
13. M. A. Fry, R. E. Durret, G. P. Ganong, D. A. Matuska, M. D. Stucker, B. S. Chambers, C. E. Needham, and C. D. Westmoreland, "The HULL Hydrodynamics Computer Code," US Air Force Weapons Laboratory Technical Report 76-183, September 1977, (UNCLASSIFIED).
14. P. W. Lunn, H. J. Happ III, and C. W. Needham, "Development of an Artificial Viscosity Function," US Air Force Weapons Laboratory Technical Report 77-53, September 1977, (UNCLASSIFIED).
15. R. D. Richtmyer and K. W. Morton, "Difference Methods for Initial Value Problems," 2d Ed., Interscience Publishers, Inc., New York, New York, 1967, pp. 311-317.

APPENDIX A
SOLUTION FOR SHOCK TUBE WITH CLOSED END

The following is a summary of the flow conditions for the 34.5 kPa (5.0 psi) step shock described in the section "Reference Problem" and used in the HULL and BAAL computations. The shock is assumed to have been produced in a shock tube having a high-pressure reservoir and a low-pressure reservoir initially in thermal equilibrium with one another, with the fluid in each reservoir at rest. The high-pressure reservoir corresponds to region 3 in Figure 1, and the low-pressure reservoir to region 1. The shock tube is assumed to be closed at both ends.

At some time, t' , after the diaphragm separating the high- and low-pressure reservoirs has been removed, a right-traveling shock wave has developed and is moving into region 1, producing shocked region 2. Simultaneously, a left-traveling expansion fan has developed and is moving into region 3, producing the expanded, accelerated region 4. Regions 2 and 4 are adjacent to one another. They have matching pressure and normal velocity components across their common boundary, but will, in general, have different densities and specific internal energies. Hence, this boundary is a discontinuity, called a contact discontinuity or contact surface. At some time, t'' , the shock reflects from the closed right end of the shock tube, creating a left-traveling reflected shock wave with region 5 behind it.

For the reference problems $T_1 = 288.2 \text{ }^{\circ}\text{K}$, $p_1 = 101.3 \text{ kPa}$, and $\rho_1 = 1.225 \text{ kg/m}^3$. The gas in both regions 1 and 3 is assumed to be air, and is further assumed to be a polytropic gas with $\gamma = 1.4$. The shock has an overpressure of 34.5 kPa. Table A.1 contains a fairly complete description of the five regions, using numerical values taken to slightly higher accuracy than the nominal values used in the text.

The computational grid was set up using the conditions in region 1 for the undisturbed ambient air, and those in region 2 for the shocked air. The conditions in region 5 represent the region behind the reflected shock prior to the arrival of any expansion waves.

Table A.1. Complete Solution, Shock Tube with Closed End

Parameter	FLOW FIELD REGION					units
	1	2	3	4	5	
γ	1.4	1.4	1.4	1.4	1.4	—
R (SI)	88.596	88.596	88.596	88.596	88.596	J/Kg °K
R (ENG)	53.352	53.352	53.352	53.352	53.352	ft-lbf/1bm °R
p (SI)	1.0133×10^2	1.3580×10^2	1.8441×10^2	1.3580×10^2	1.7986×10^2	kPa
p (ENG)	1.4696 $\times 10^1$	1.9696 $\times 10^1$	2.6746 $\times 10^1$	1.9696 $\times 10^1$	2.6086 $\times 10^1$	1bf/in ²
p_0 (SI)	1.0133×10^2	1.3984×10^2	1.8441×10^2	1.4060×10^2	1.7986×10^2	kPa
p_0 (ENG)	1.4696 $\times 10^1$	2.0282 $\times 10^1$	2.6746 $\times 10^1$	2.0393 $\times 10^1$	2.6086 $\times 10^1$	1bf/in
ρ (SI)	1.2249	1.5088	2.2293	1.7918	1.8429	kg/m ³
ρ (ENG)	7.6468×10^{-2}	9.4190×10^{-2}	1.3917×10^{-1}	1.1186×10^{-1}	1.1505×10^{-1}	lbm/ft ³
ρ_0 (SI)	1.2249	1.5407	2.2293	1.8368	1.8429	kg/m ³
ρ_0 (ENG)	7.6468×10^{-2}	9.6182×10^{-2}	1.3917×10^{-1}	1.1467×10^{-1}	1.1505×10^{-1}	lbm/ft ³
T (SI)	2.8818 $\times 10^2$	3.1356×10^2	2.8818×10^2	2.6403×10^2	3.3998×10^2	°K
T (ENG)	5.1872 $\times 10^2$	5.6440×10^2	5.1872×10^2	4.7526×10^2	6.1196×10^2	°R
T_0 (SI)	2.8818×10^2	3.1619×10^2	2.8818×10^2	2.6667×10^2	3.3998×10^2	°K
T_0 (ENG)	5.1872 $\times 10^2$	5.6914×10^2	5.1872×10^2	4.8000×10^2	6.1196×10^2	°R
I (SI)	2.0680 $\times 10^5$	2.2495×10^5	2.0680×10^5	1.8947×10^5	2.4398×10^5	J/kg
I (ENG)	6.9187×10^4	7.5259×10^4	6.9186×10^4	6.3388×10^4	8.1625×10^4	ft-lbf/1bm
u (SI)	0.	7.2771×10^1	0.	7.2771×10^1	0.	m/s
u (ENG)	0.	2.3875 $\times 10^2$	0.	2.3875 $\times 10^2$	0.	ft/s
c (SI)	3.4031×10^2	3.5497×10^2	3.4031×10^2	3.2574×10^2	3.6963×10^2	m/s
c (ENG)	1.1165×10^3	1.1646×10^3	1.1165×10^3	1.0687×10^3	1.2127×10^3	ft/s
M	0.	2.0501×10^{-1}	0.	2.2340×10^{-1}	0.	—

APPENDIX B
DETAILED DISCUSSION OF SEMIEMPIRICAL MODELS

A. Front Face

The Technical Manual's method for computing the loading on the front face of a rectangular parallelepiped (such as the shelter) is based on an assumed clearing time t_c , where

$$t_c = \frac{3h}{c_5}. \quad (B.1)$$

Here, c_5 is the sound speed on the front face of the shelter after the shock has reflected from it. The value to be used for h is the smaller of either the height of the shelter or one half the width. The clearing time t_c is "... the time required to clear the front wall of reflection effects"². During this time, the average overpressure on the front face decreases from the peak reflected overpressure to a value, in the case of an exponentially decaying wave, computed by²

$$\bar{p}_f^* = p^*(t)_f + 0.85 \frac{1}{2} \rho_2 u_2^2. \quad (B.2)$$

In Equation (B.2), ρ_2 is the density behind the incident shock, u_2 is the particle velocity behind the incident shock, and $p^*(t)_f$ is the time-dependent value of the incident shock overpressure at the plane of the front face,

$$p^*(t)_f = (p_2 - p_1) \left[1 - \left(\frac{t - t_d}{t_{pos}} \right) \right] e^{-(t-t_d)/t_{pos}}. \quad (B.3)$$

Here, p_1 is the absolute pressure ahead of the shock and p_2 is the absolute pressure behind the shock. Also, t is the time measured after shock arrival at the front face; t_d is the time required to travel to the surface under consideration, which in this case is the front surface, so $t_d = 0.0$; t_{pos} is the duration of the positive phase. For a stop shock, Equation (B.3) reduces to

$$p^*(t)_f = p_f^* = (p_2 - p_1), \quad (B.4)$$

so Equation (B.2) becomes

$$p_f^* = p_2 - p_1 + 0.85 \frac{1}{2} \rho_2 u_2^2. \quad (B.5)$$

For the reference shock (See Section II and Appendix A.), the peak reflected overpressure on the front face of a rectangular parallelepiped is $(p_5 - p_1)$.

Taylor¹ suggested an alternate method to estimate the loading on the front face of an obstacle, based on the number of rarefaction wave crossings. For a 3-D object such as the shelter, there will be a succession of rarefaction waves originating from the top of the front face and reflecting from the bottom boundary, plus a succession of rarefaction waves originating from the side face and reflecting from the symmetry plane. The reflected waves will also be expansion waves. In an actual occurrence of loading through shock diffraction, there is considerable interaction between the crossing expansion waves. Because Taylor intended that the method be a simple approximation, the waves are assumed not to interfere with one another. As a further simplification, the rarefaction wave speeds are assumed to be equal to the sound speed in the reflection region immediately after the incident shock reflects from the front face.

Using Taylor's method, the required crossing time for an expansion wave running from the top to the bottom of the front face is computed, as is that for an expansion wave running from the side edge to the symmetry plane. For each expansion wave crossing, the average overpressure on the front face is then computed as a percentage of the initial reflected overpressure on the front face ($p_5 - p_1$), as shown in Table 1 of this report.

B. Back Face

The time required for the incident shock wave to arrive at the plane of the back wall is

$$t_d = \frac{D}{W_i}, \quad (B.6)$$

where D is the shelter depth, and W_i is the velocity of the incident shock. The rise time² required for the pressure on the back face to go from ambient at time t_d to its peak average value is

$$(t_b)_{rise} = \frac{ah}{c_i}, \quad (B.7)$$

where $a = 4.0$, c_i is the sound speed ahead of the shock, and h is defined as before. The peak average overpressure² on the back face is

$$(p_b^*)_{max} = p^*(t)_b \left(\frac{1}{2} \right) \left[1 + (1 - \beta) e^{-\beta} \right], \quad (B.8)$$

where $p^*(t)_b$ is the incident shock wave overpressure at the time it arrives at the plane of the back face (See Equation (B.3).), and

$$\beta = \frac{1}{2} \frac{[p^*(t)_f]_{t=0}}{p_1} . \quad (B.9)$$

Here $[p^*(t)_f]_{t=0}$ is the incident shock wave overpressure at the time it arrived at the plane of the front face, and p_1 is the absolute pressure ahead of the shock. For the step shock considered here,

$$[p^*(t)_f]_{t=0} = p^*(t)_b = (p_2 - p_1) \quad (B.10)$$

The Technical Manual model modified for a step shock implies that the average overpressure on the back face would remain at $(p_b^*)_{\max}$ indefinitely.

Taylor's data indicate that the constant α used in Equation (B.7) to compute the rise time should be changed to 2.5 from 4.0. The rise time is measured from the arrival time, t_d , of the shock at the plane of the back face to the time at which the average overpressure on the back face reaches $(p_b^*)_{\max}$. This gives a more rapid rise time on the back face than that computed by using the model in the Technical Manual.

C. Top and Side Faces

Taylor does not suggest an improved method for computing the average overpressure on the top and side faces of an object such as the shelter. The method outlined in the Technical Manual is presented here for later comparison with the results computed using the hydrodynamic computer codes. From time zero, when the incident shock wave reaches the plane of the front face of the target, to the time t_d at which the shock wave reaches the plane of the back face, the average overpressure on the top face varies linearly² from zero to

$$p_{\text{top}}^* = (p_2 - p_1) \left[0.9 + 0.1 \left(1.0 - \frac{p_2 - p_1}{p_1} \right)^2 \right] \quad (B.11)$$

for the step shock considered here. To account for vortex growth, shedding, and subsequent travel down the top face, the model predicts a local minimum in the average overpressure at the time

$$t_{\text{pmin}} = \frac{SD}{W_i} . \quad (B.12)$$

At that time, the average overpressure on the top face is computed² as either

$$\bar{p}_{top}^* = (p_2 - p_1) \left[2.0 - \left(\frac{p_2 - p_1}{p_1} + 1 \right) \left(\frac{h}{D} \right)^{1/3} \right], \quad (B.13.1)$$

or

$$\bar{p}_{top}^* = (p_2 - p_1) \left[0.5 + 0.125 \left(2 - \frac{p_2 - p_1}{p_1} \right)^2 \right], \quad (B.13.2)$$

whichever is the lesser of the two, for the step shock considered here. After this time, there is a linear rise in the average overpressure to a value in the case of a step shock of

$$\bar{p}_{top}^* = p_2 - p_1. \quad (B.14)$$

from the time t_{pmin} to a time

$$t = t_{pmin} + \frac{15 D}{W_i}. \quad (B.15)$$

According to the method outlined in the Technical Manual, the geometry of the shelter is such that the times and average overpressures for the top face also apply directly to the side face of the shelter.

APPENDIX C
COMPUTATIONAL GRIDS

Because the HULL and BAAL codes use different conventions for naming directions and indices, the BAAL results¹⁰ and the flow field description are reproduced in part using the HULL hydrocode conventions. Figure 6 of this report shows a 3-D view of the shelter in the computational flow field. Figure C.1 shows the projection of the computational grid on the front face, Figure C.2 the projection on the top face, and Figure C.3 the projection on the side face. The indicated pressure anomalies on these faces in the BAAL computation are discussed in Appendix E.

The computational grid used for the HULL code is identical with that used in the BAAL computation, except that the HULL grid has one additional plane of cells in the X direction, four additional planes of cells in the Y direction, and three additional planes of cells in the Z direction, all added at the upper extreme of distance in the respective directions. Table C.1 is a tabulated list of cell vertex locations versus computational grid indices. The single plane of cells was added to the HULL grid in the X direction to satisfy a code requirement that the number of cells in the X direction be odd. The extra planes of cells were added in the Y and Z directions for the HULL grid to allow the code to process a longer simulated flow time prior to the possible arrival at the shelter of artificial signals reflecting from the transmissive boundaries of the computational flow field.

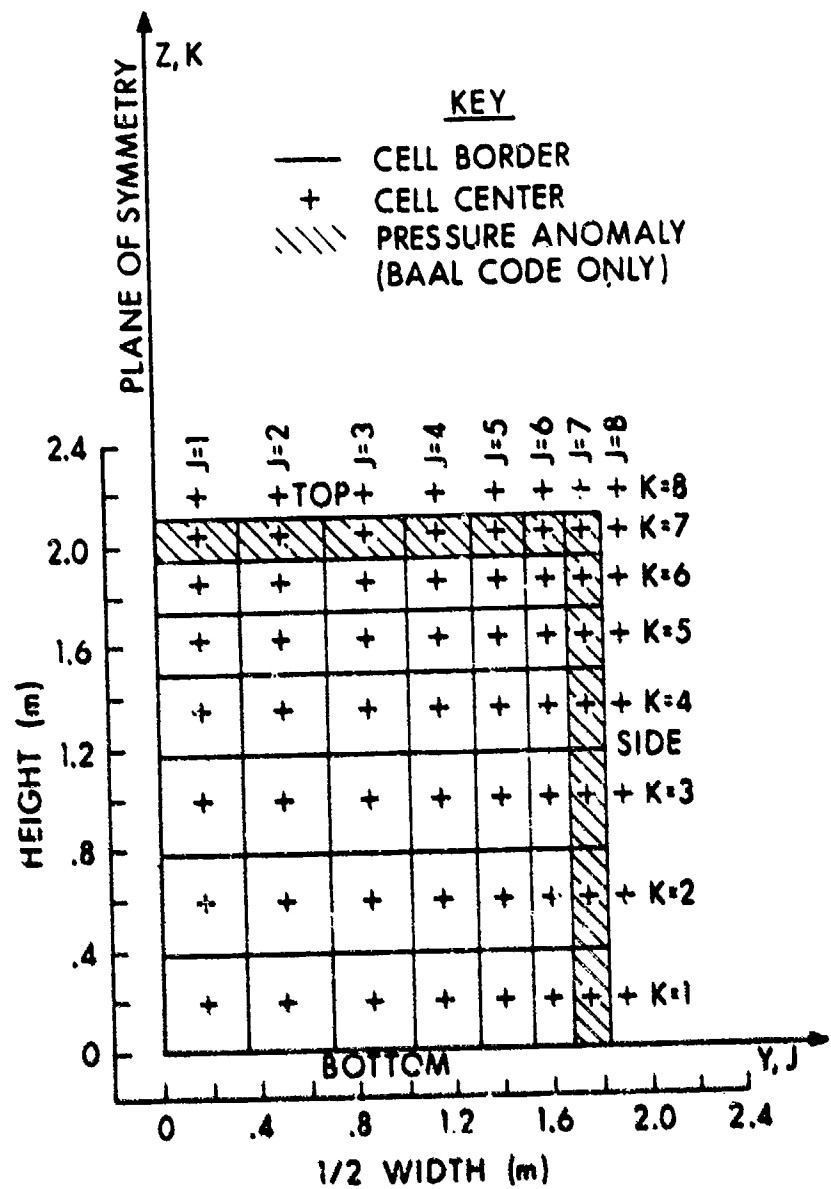


Figure C.1. Computational grid on front face.
(Identical back face, including pressure anomalies.)

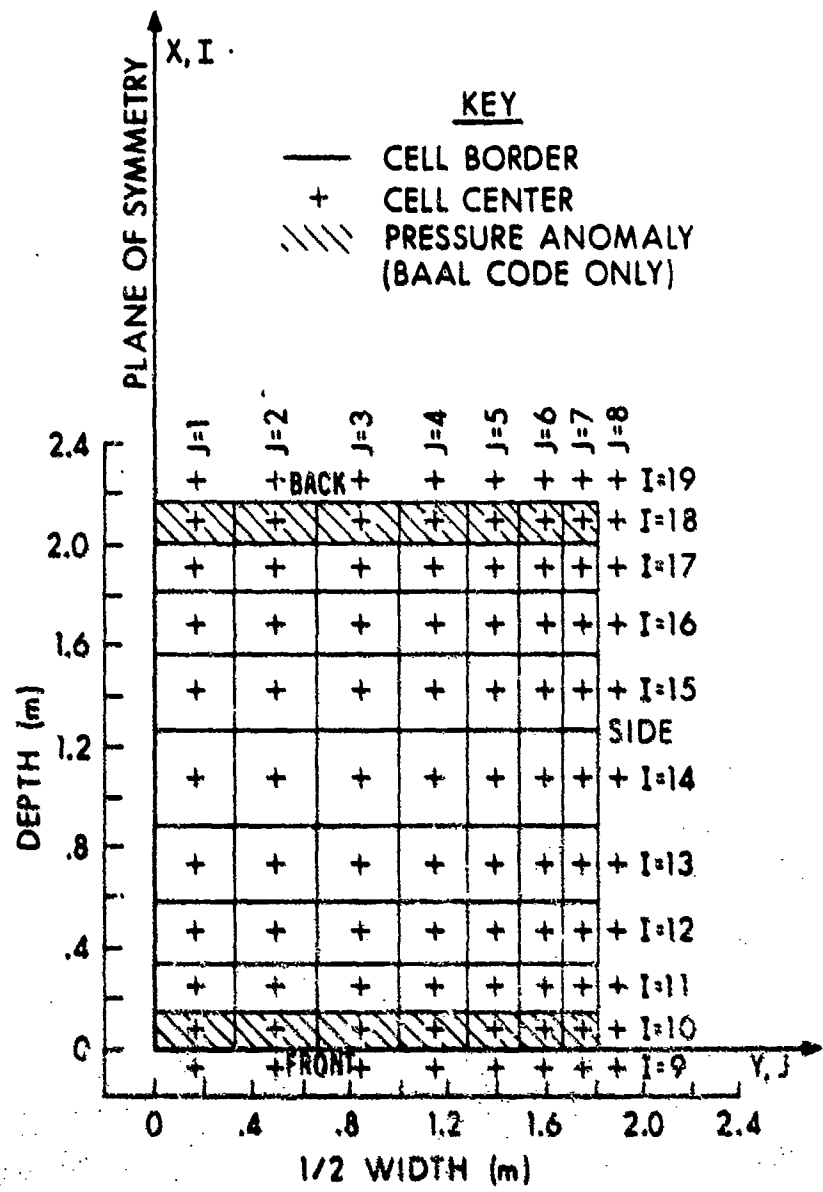


Figure C.2. Computational grid on top face.

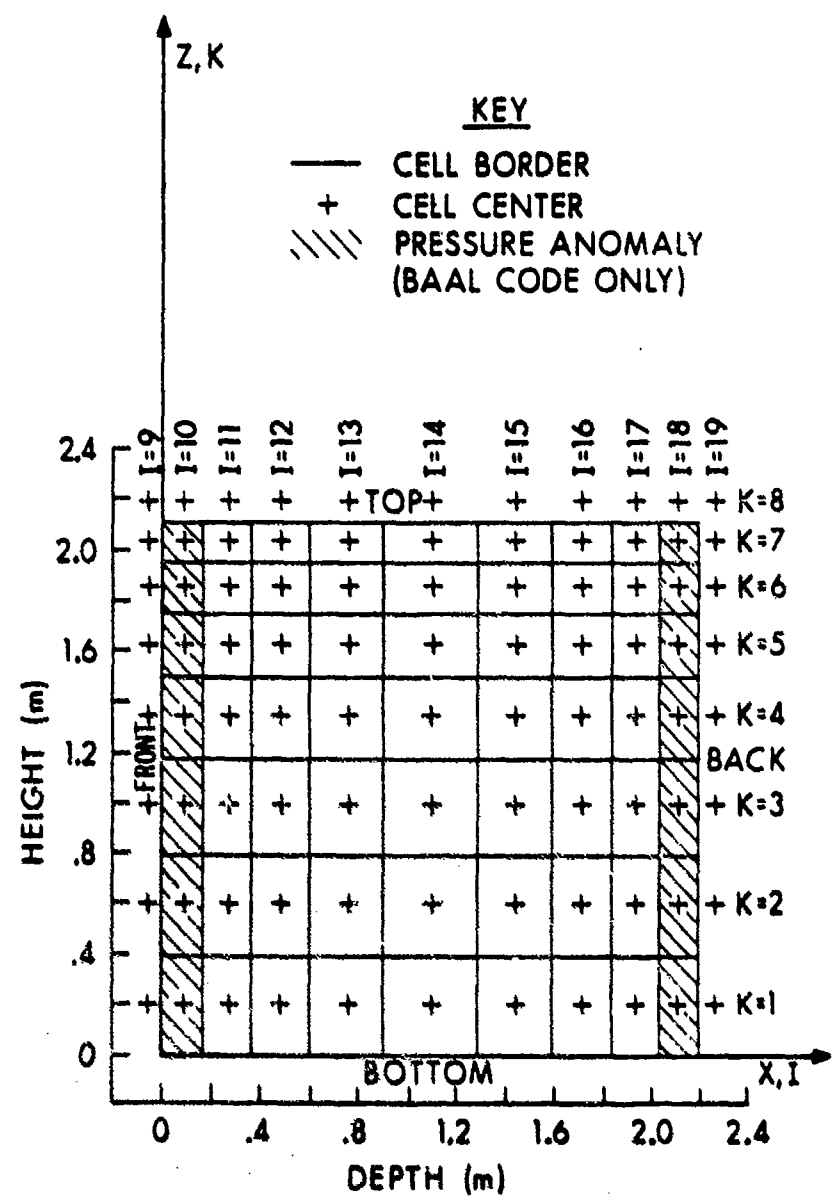


Figure C.3. Computational grid on side face.

Table C.1. Cell Vertices, HULL and BAAL Grids

I	X (m)	J	Y (m)	K	Z (m)
Origin	0.0000	Origin	0.0000	Origin	0.0000
1	1.9622	1	0.3376	1	0.3933
2	3.3154	2	0.6752	2	0.7865
3	4.2487	3	1.0128	3	1.1798
4	4.8923	4	1.2828	4	1.4944
5	5.3520	5	1.4989	5	1.7461
6	5.6804	6	1.6717	6	1.9474
7	5.9233	7	1.8100	7	2.1085
8	6.1176	8	1.9483	8	2.2696
9	6.2731	9	2.1332	9	2.4850
10	6.4285	10	2.3805	10	2.7732
11	6.6228	11	2.7383	11	3.1900
12	6.8657	12	3.2744	12	3.8145
13	7.1693	13	4.1965	13	4.7499
14	7.5488	14	5.6671	14	6.2012
15	7.8524	15	8.0129	15	8.4529
16	8.0953	16*	10.3587	16*	10.7047
17	8.2896	17*	12.7044	17*	12.9564
18	8.4451	18*	15.0502	18*	15.2081
19	8.6005	19*	17.3959		
20	8.7948				
21	9.0377				
22	9.3661				
23	9.8258				
24	10.4694				
25	11.4027				
26	12.7559				
27	14.7181				
28	16.6803				
29	18.6425				
30	20.6047				
31*	22.5668				

* Added cell, HULL grid only

APPENDIX D
OTHER LOADING FUNCTIONS

Figure D.1 shows the gage positions that Taylor¹ used in estimating the loading for the front and back faces of a three-dimensional rectangular parallelepiped tested in the BRL shock tube. The experimentally measured overpressure histories for these points were used as a basis for evaluating the BAAL computation by Gentry et al⁸. Point A is located at the centroid of triangle FGO, point C at the centroid of triangle EOH, and point D at the centroid of triangle EFO. Taylor's function for estimating the average overpressure on either the front or back face is

$$\bar{p}^* = \frac{2p_A^* + p_C^* + p_D^*}{4}, \quad (D.1)$$

where p_A^* is the overpressure at point A, p_C^* is the overpressure at point C, and p_D^* is the overpressure at point D.

Ethridge¹² has proposed empirical correlation functions for the front and rear surfaces of a rectangular parallelepiped. For the average overpressure on the front surface of a S-280 shelter struck by the reference 34.5 kPa step shock, Ethridge's function reduces to

$$\bar{p}_f^* = 38.51 + (40.02) e^{(-.3288)(374.4 t)} (1.412 + .1667 e^{-44.47 t}) \quad (D.2)$$

Figure D.2 shows a comparison of the average overpressure on the front face computed with Ethridge's empirical function, HULL B, and Taylor's weighted function shown in Equation (D.1). The overpressure histories for points A, C, and D were computed using spatially interpolated values for those points in the HULL B computation. Figure D.2 indicates that Taylor's weighted function for those three points gives an excellent approximation to the average overpressure for the front face. Ethridge's empirical function also shows good agreement with the computed solution, especially at late time. At early time, Ethridge's function is probably more reliable than the HULL B solution because it is based on the theoretical reflected value at time zero and is not subject to the kind of numerical oscillation exhibited by the HULL solution. However, it does not show the apparent over-relief of pressure found both experimentally and computationally near 10 ms.

Figure D.3 shows the average overpressure on the back face of the shelter computed with Ethridge's empirical function, Taylor's weighted function, and HULL B. Ethridge's empirical function for the average overpressure on the back face of the shelter struck by the reference shock reduces to

$$\bar{p}_b^* = (.9300) \left[1 - e^{-161.2 t} (1 + 5656 t^2) \right]. \quad (D.3)$$

Taylor's weighting function, Equation (D.1), is the same for the back face as for the front face. The overpressures for points A, C, and D on the back face were computed by performing linear interpolations in the HULL B solution in the same manner as was done for the corresponding points on the front face. Ethridge's empirical function shows good general agreement with the HULL B computation, but does not show the peak and local minimum suggested in Figure 8 of this report and by the proposed model. It also seems to load the back face more rapidly. The weighted function of Equation (D.1) seems to be a reasonable approximation to the full solution except that it overpredicts the loading near the peak. This overprediction is especially interesting because it is of essentially the same nature as the overprediction of Taylor's weighted function¹, as shown by Gentry et al⁸. Figure 14 of their report, reproduced here as Figure D.4, compares the experimentally measured overpressures, the complete BAAL solution, and the interpolated values for analogous points A, C, and D on a rectangular parallelepiped tested in the BRL shock tube. The solid line represents the weighted average for the experimentally measured values at points A, C, and D. The dashed line with the x's represents the weighted average of the overpressures at points A, C, and D found by performing linear interpolation using a BAAL hydrocode computation. The dashed line with the o's represents the average overpressure on the back face using the BAAL computation for the entire face.

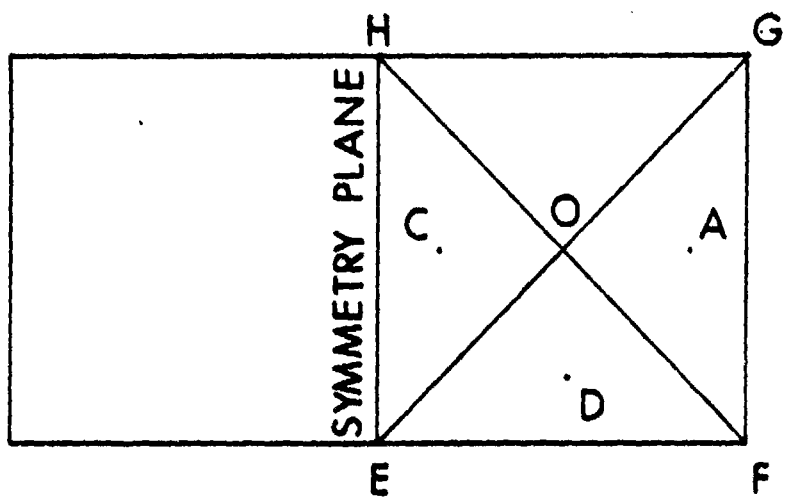


Figure D.1. Taylor's gage positioning for front and back face loading on a rectangular parallelepiped.

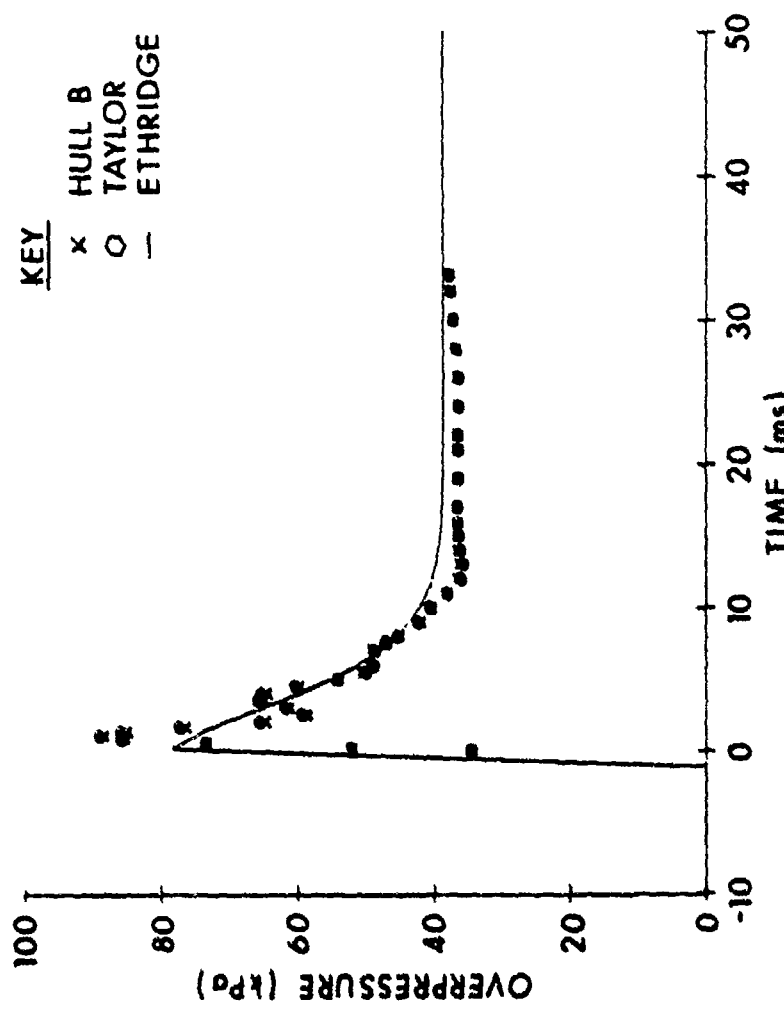


Figure D.2. Front face average overpressure.

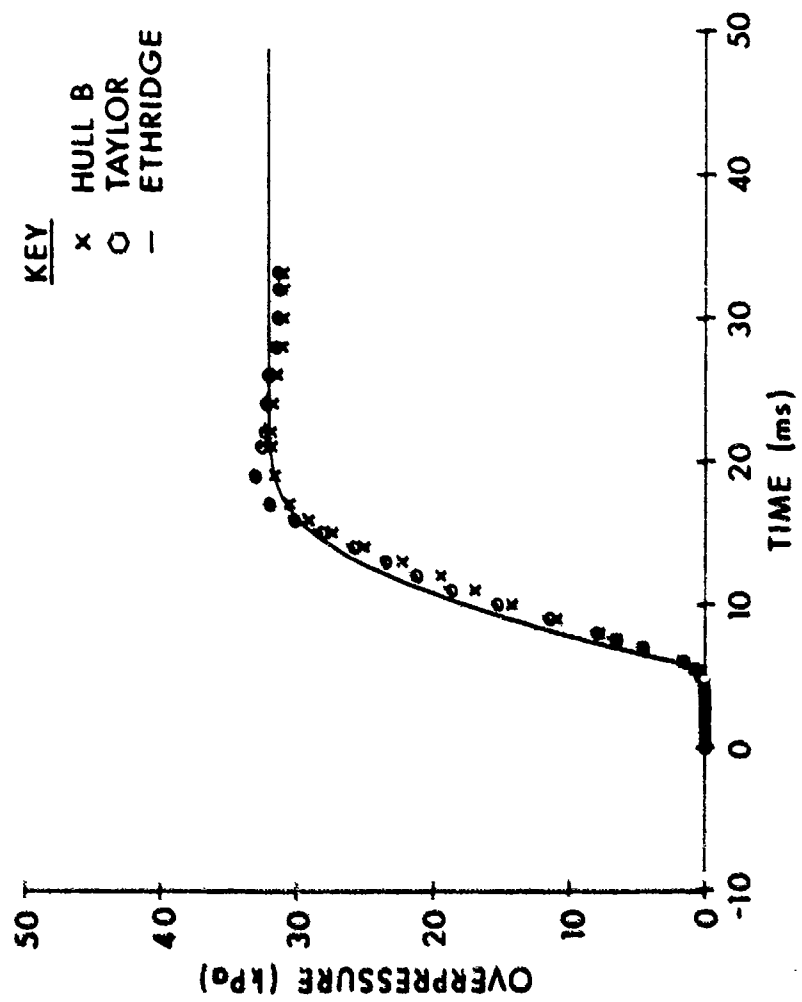


Figure D.3. Back face average overpressure.

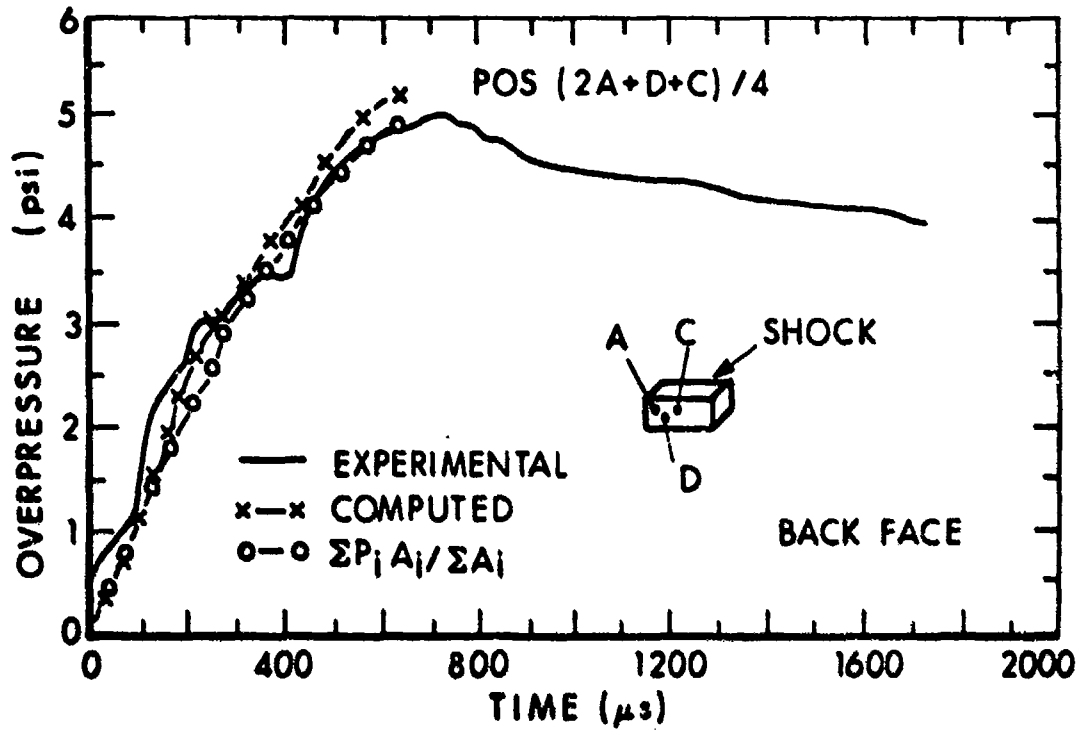


Figure D.4. Average overpressure on the back face of a rectangular parallelepiped being struck by a 5.0 psi step shock. (Reproduced from Gentry et al.⁸.)

APPENDIX E
DETAILED COMPARISON OF HYDROCODE RESULTS

A. Front Face

As may be seen by comparing Figures C.1, C.2, and C.3 in Appendix C with Figures 2a, 2b, and 2c in the earlier study¹⁰, additional apparent anomalies have been identified in the BAAL computation during the current analysis. The anomalies on the front face of the shelter are manifested as excessively high pressures in the topmost row of flow field cells (indices $I = 9$, $J = 1$ through 7, $K = 7$, or $(9,1-7,7)$) and the right-most column of cells $(9,7,1-7)$. Figure E.1 shows overpressure histories for cell $(9,7,4)$, a flow field cell in the right-most column of cells on the shelter's front face, four cells up from the bottom. Except for very early in the diffraction phase, the BAAL overpressures for the cells in that column, as cell $(9,7,4)$ typifies, are in general significantly larger than those for the two HULL computations. Correspondingly, Figure E.2 shows an even more severe effect in the overpressure history for cell $(9,7,7)$, the flow field cell on the upper right corner of the front face. Except in those areas where apparent anomalous behavior is exhibited in the BAAL solution for the front face, the relative agreement in the BAAL and HULL computations is more accurately characterized by the overpressure history of cell $(9,3,3)$, a cell located near the center of the one-half shelter front face, as shown in Figure E.3. Here, the BAAL computation shows the more typical increase in overpressure above that for the HULL computations for late time ($t > 20$ ms).

B. Back Face

The pressure anomalies in the BAAL computation for the back face of the shelter are in essentially the opposite sense from those on the front face. The overpressures for the top row of flow field cells $(19,1-7,7)$ and the outermost column of flow field cells $(19,7,1-7)$ are significantly less than those computed by using HULL. Figure E.4 shows the overpressure history of cell $(19,3,7)$, one of the flow field cells along the top row of cells on the shelter's back face. It shows the typical late-time overpressure disagreement between the BAAL computation and the HULL computations for that row of flow field cells. Figure E.5 shows a similar, typical disagreement between the BAAL and HULL computations for a flow field cell in the outermost column of cells on the back face. Figure E.6 shows the overpressure history of flow field cell $(19,3,3)$, situated approximately on the center of the one-half back face. The relative performance of the BAAL and HULL computations shown in Figure E.6 typifies that for the flow field cells on the back face, but not at the outer edges of the back face.

C. Top Face

Apparent pressure anomalies in the BAAL computation also exist on the top and side faces, and are quite similar to those on the front and back faces. Figure E.7 shows the overpressure history of flow field cell $(10,3,8)$, the third cell in the Y direction from the

symmetry plane in the first row of flow field cells along the top face. Here, the overpressure as computed by BAAL is consistently much less than that computed by either of the two HULL computations. The overpressure history of flow field cell (9,3,7), the top flow field cell in the third column of cells up the front face (not shown in this report), shows relative values of overpressure between the BAAL and HULL computations similar to those shown in Figures E.4 and E.5. This is part of a consistent pattern of the main differences in the overpressure histories in the HULL and BAAL computations for flow field cells just before and just after a 90-degree expansion corner. The BAAL computation shows consistently higher values of overpressure than do the HULL computations in the flow field cells on the shelter surface just upstream of the 90-degree expansion corner, and consistently lower values on the shelter surface just after the expansion. Figure E.8 shows the overpressure history of flow field cell (18,3,8), the third cell in the Y direction from the symmetry plane in the last row of flow field cells along the top face. Here the overpressure from the BAAL computation is consistently greater than from the HULL computations. Figures E.1 and E.2 show similar results for analogous front face cells. Figure E.9 shows the overpressure history of flow field cell (14,7,8), the outermost cell in the fifth row of flow field cells down the top face. This 90-degree corner of the shelter is along a line parallel rather than perpendicular to the flow; hence there are no large pressure or velocity gradients around this cell as there would be for a similar corner which is oriented perpendicular to the flow. As may be seen in Figure E.9, the agreement between the HULL and BAAL codes is generally good, except for the delayed, enhanced peak for HULL A; the cause of this discrepancy was discussed earlier in this report. Figure E.10 for flow field cell (14,3,8), located near the center of the half of the top face, shows the typical good agreement between the HULL and BAAL computations for flow field cells on the top face but not immediately adjacent to the 90-degree expansion corner regions.

D. Side Face

Figure E.11 shows the overpressure history of flow field cell (10,8,4), the fourth cell up from the bottom boundary in the first column of flow field cells along the side face. This cell is on the downstream side of the 90-degree expansion corner from the front face to the side face. The BAAL overpressure values are consistently less than the HULL values, showing the same behavior as that for analogous flow field cells shown in Figures E.4, E.5, and E.7. Figure E.12 shows the overpressure history of flow field cell (18,8,4), the fourth cell up from the bottom boundary in the last column of flow field cells along the side face. This cell is on the upstream side of the 90-degree expansion corner from the side face to the back face. As is the case for the analogous flow field cells in Figures E.1, E.2, and E.5, the BAAL overpressure values are consistently greater than the values from either of the HULL computations. Figure E.13 shows the overpressure history of flow field cell (14,8,3), the fifth cell along the third

row of flow field cells up from the bottom boundary on the side face. As is the case for the analogous flow field cell shown in Figure E.9, the BAAL and HULL calculations show good general agreement, as do the flow field cells away from the edges of the top and side shelter faces (such as those shown in Figures E.14 and E.10).

E. General View

Figure E.15 shows an exploded view of the S-280 shelter, indicating the pattern by which the BAAL computation of overpressure on the shelter differs from that computed by HULL. The BAAL computation of overpressure is consistently higher than that computed by HULL for flow field cells on the shelter surfaces just upstream of a 90-degree expansion corner, and consistently lower for flow field cells on the shelter surface just downstream of a 90-degree expansion corner.

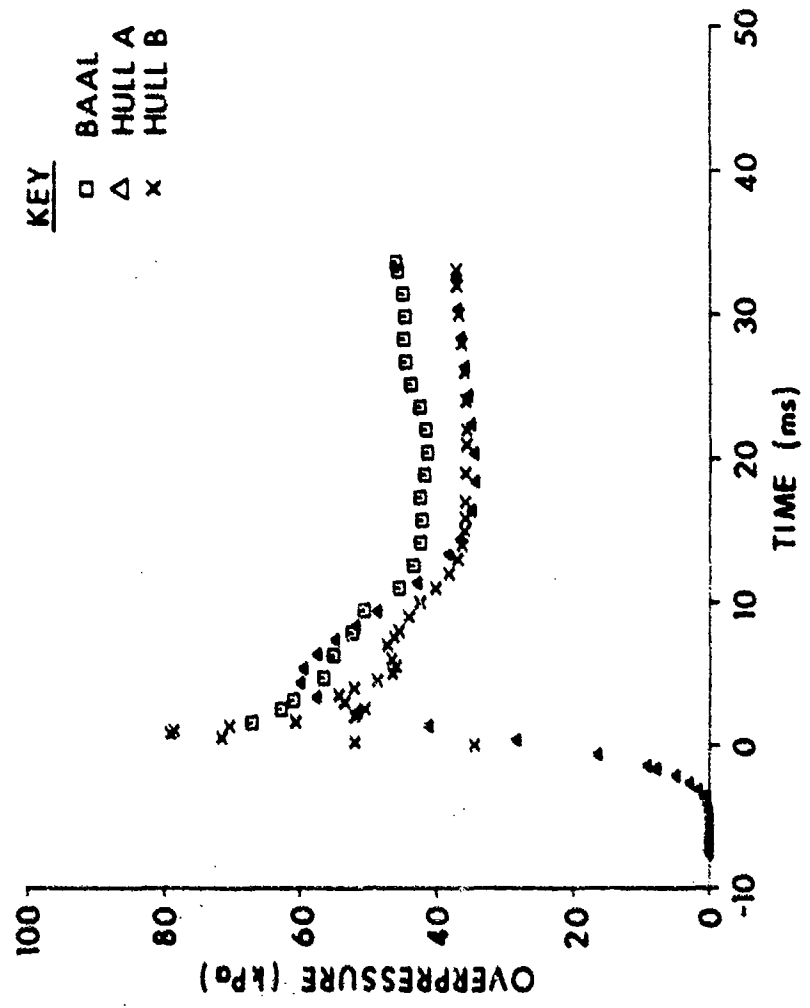


Figure E.1. Overpressure for front face cell (9,7,4).

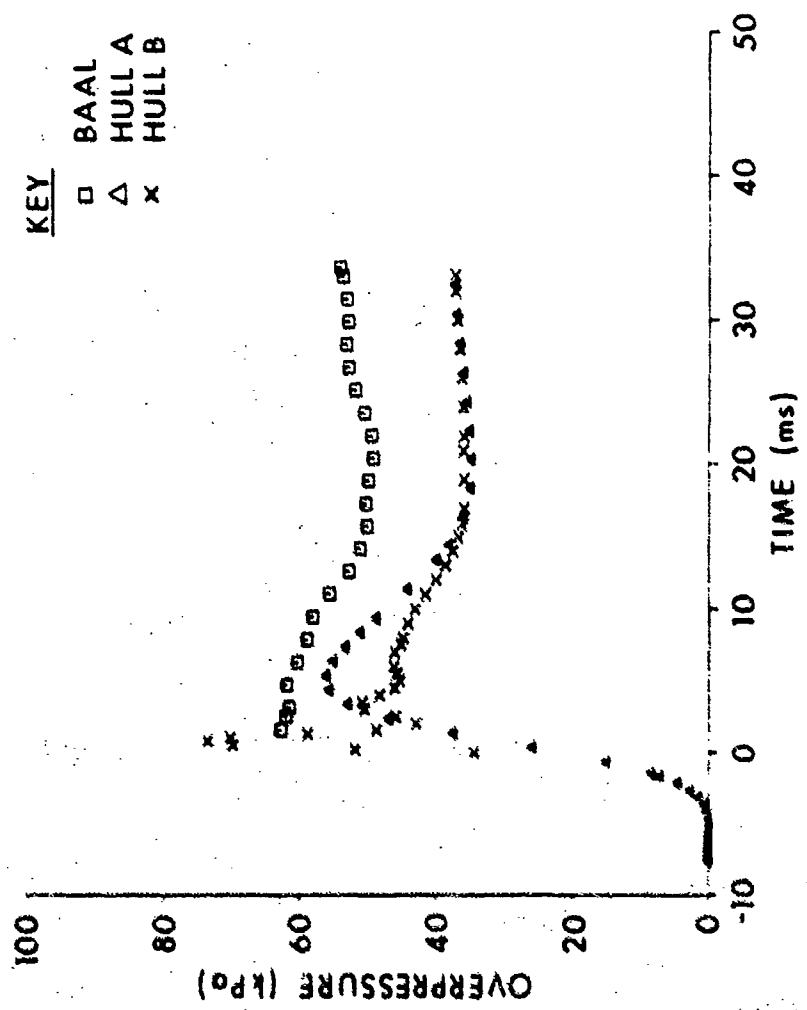


Figure I.2. Overpressure for front face cell (9,7,7).

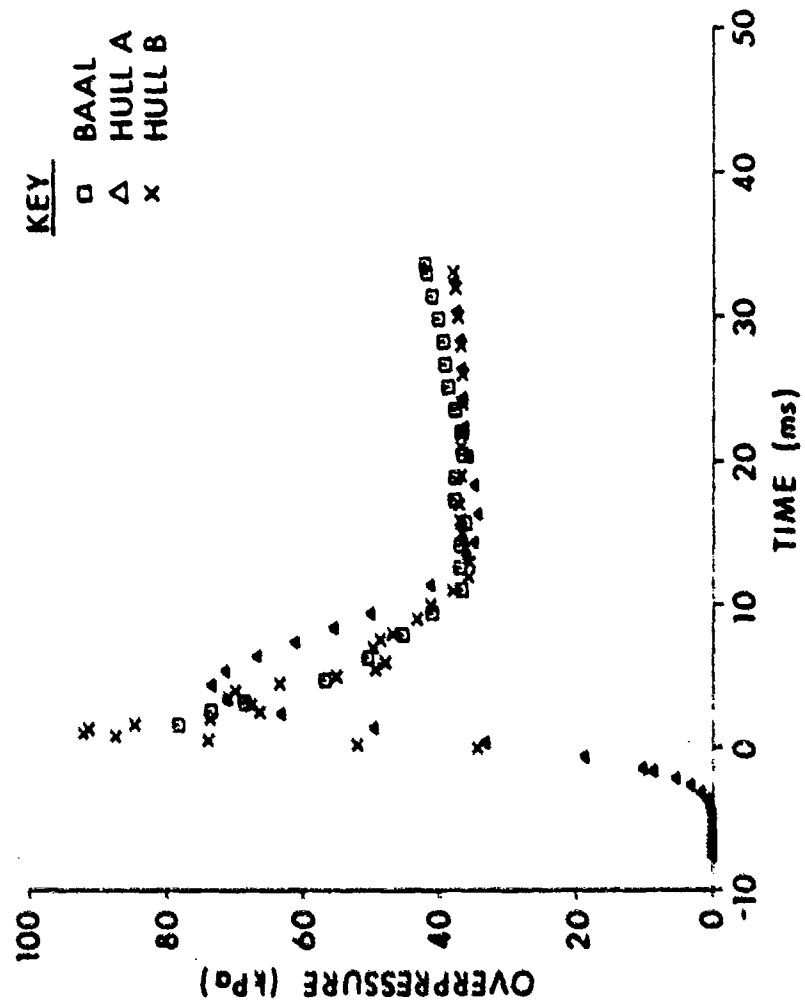


Figure E.3. Overpressure for front face cell 11 (9,3,3).

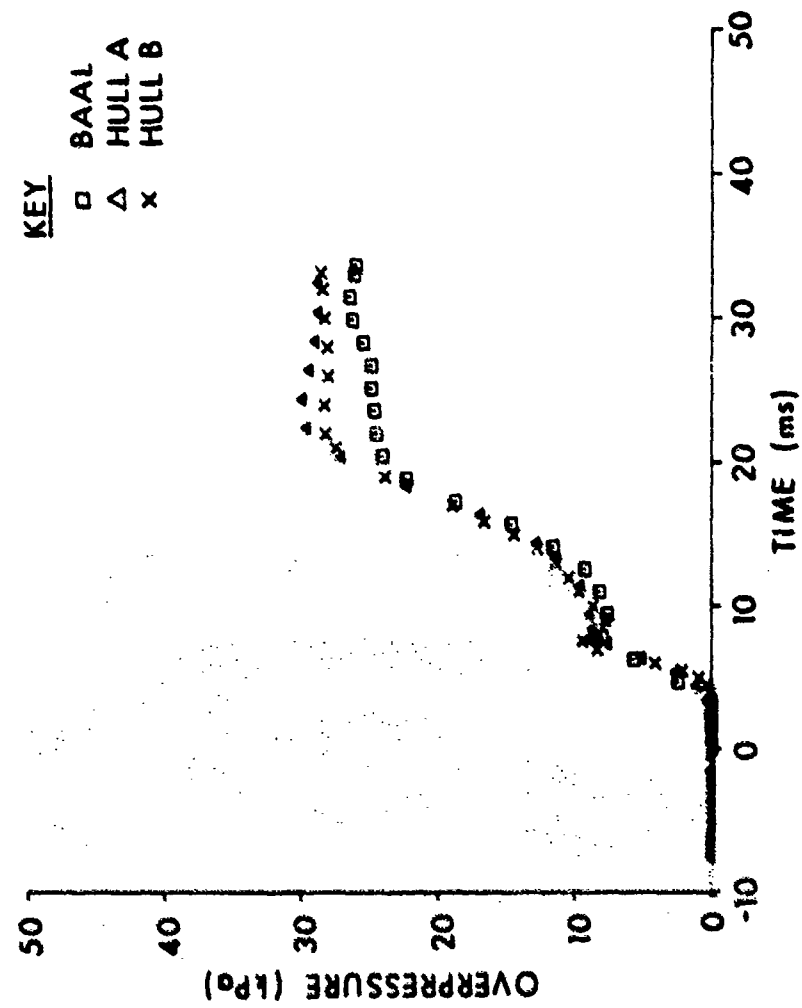


Figure E.4. Overpressure for back face cell (19,3,7).

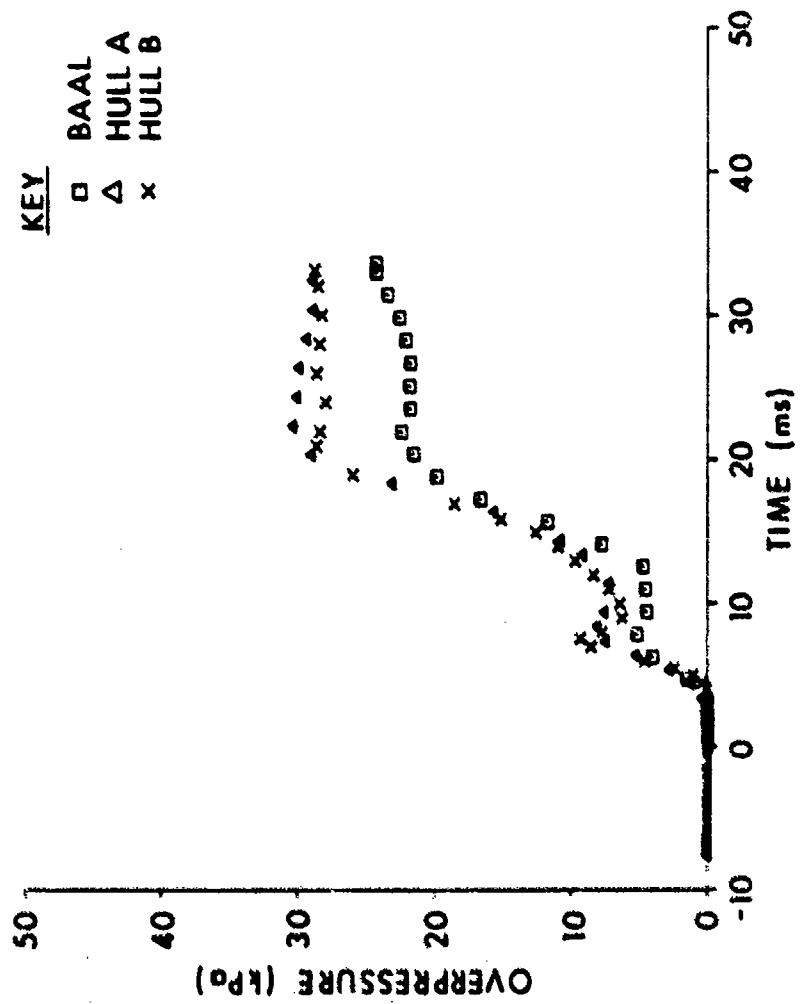


Figure F.5. Overpressure for back face cell (19,7,3).

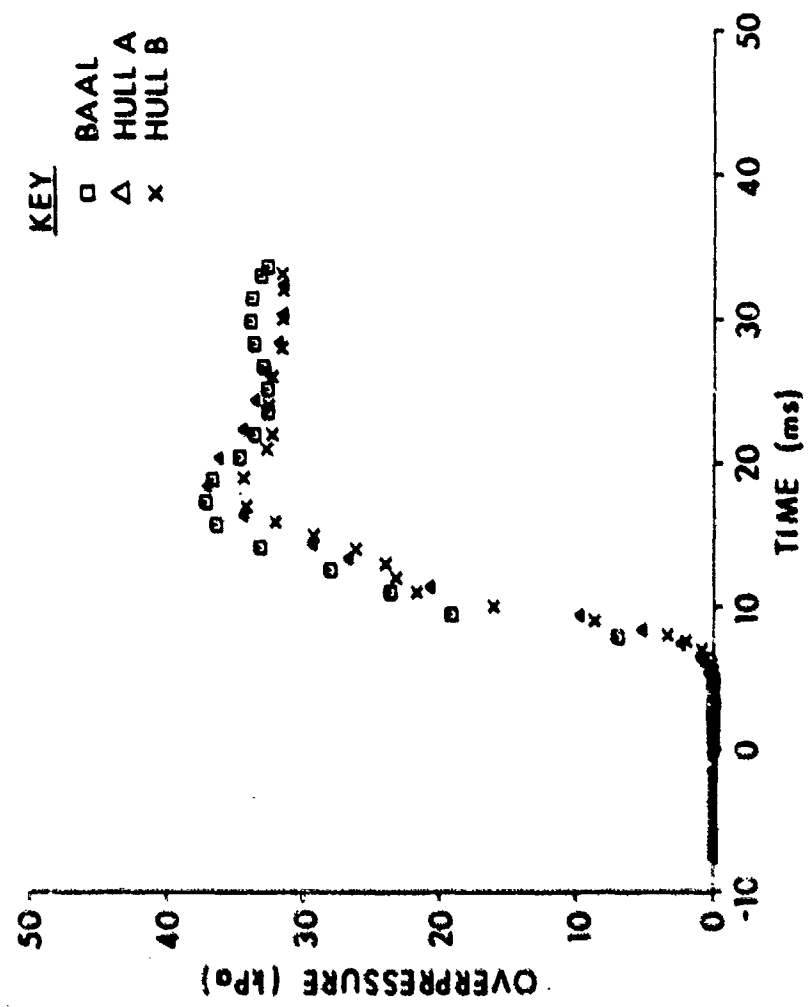


Figure E.6. Overpressure for back face cell (19,3,3).

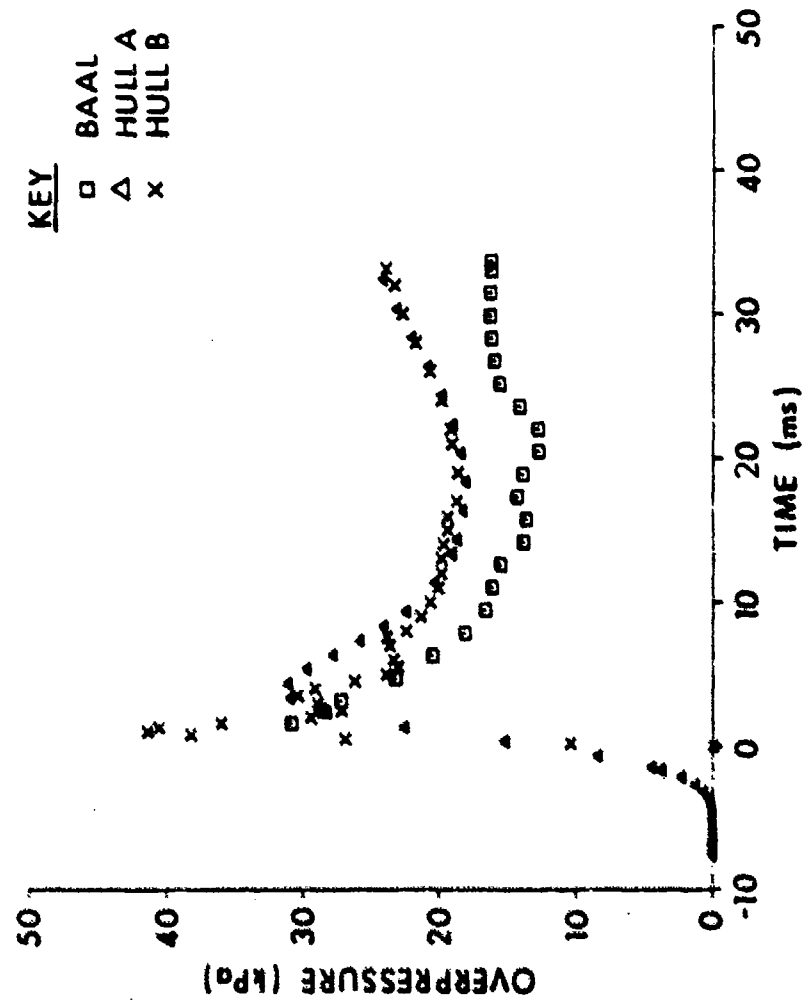


Figure E.7. Overpressure for top face cell (10,3,8).

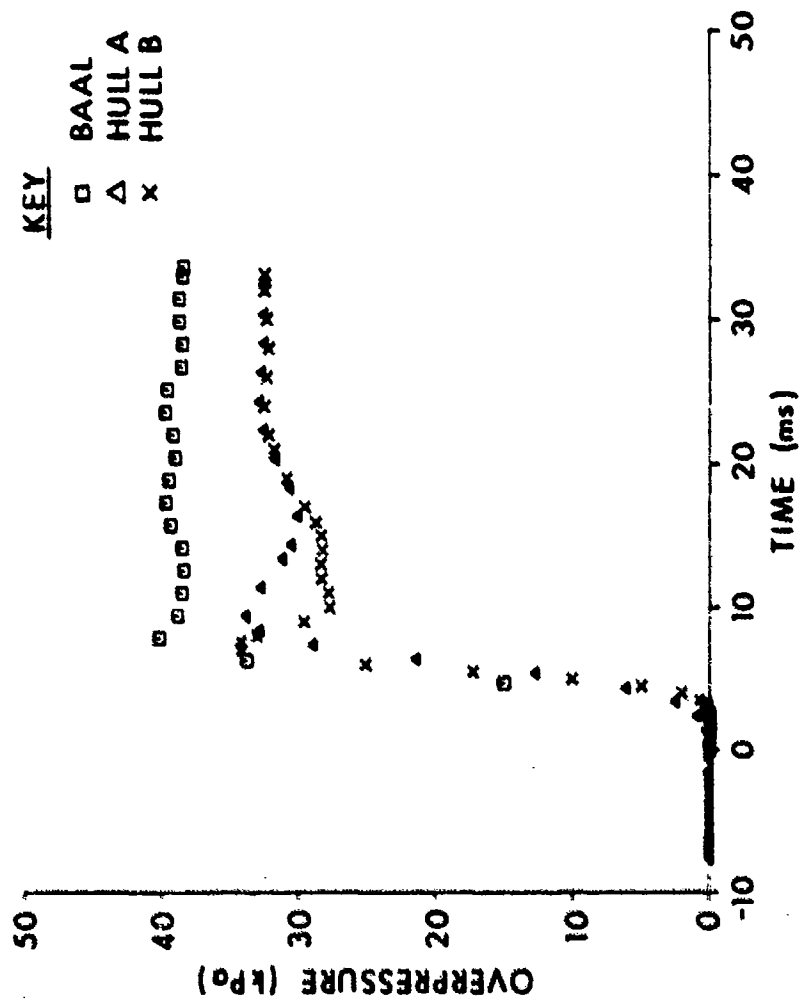


Figure E.8. Overpressure for top face cell (18,3,8).

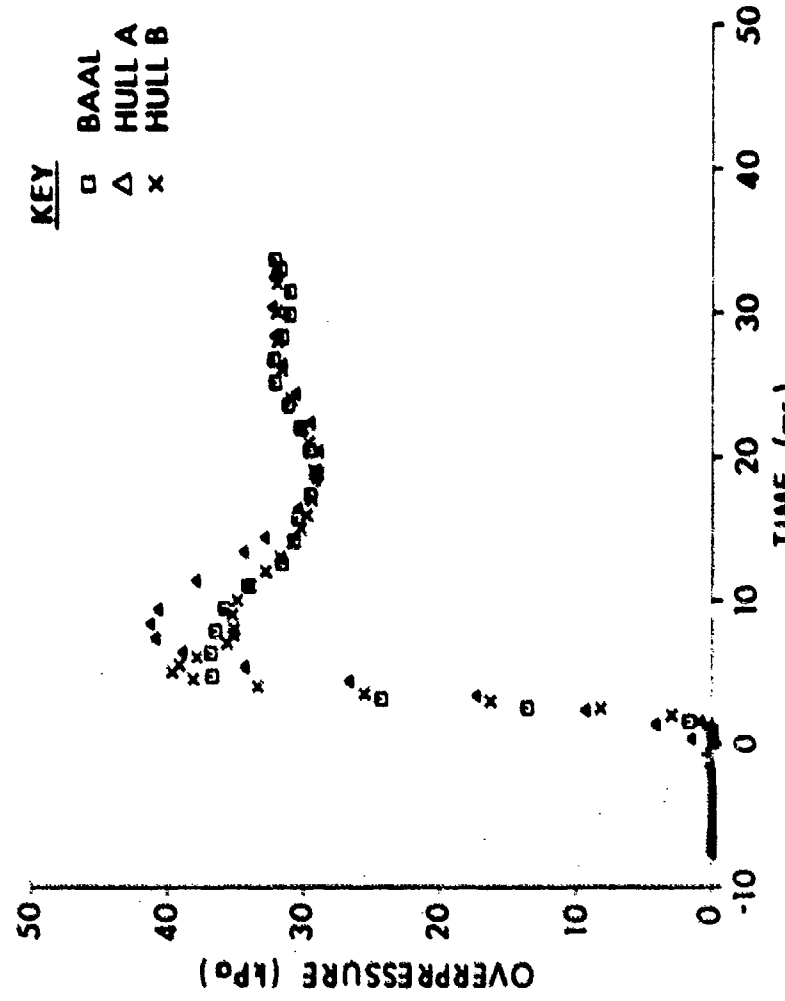


Figure E.9. Overpressure for top face cell (14,7,8).

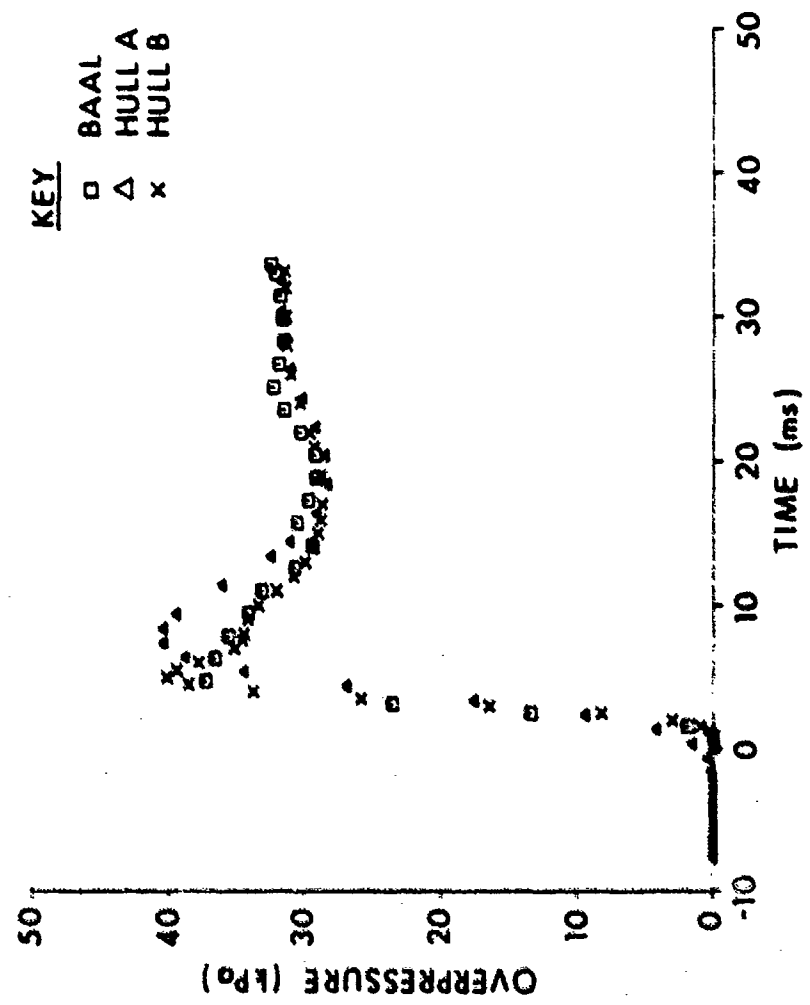


Figure F.10. Overpressure for top face cell (14,3,8).

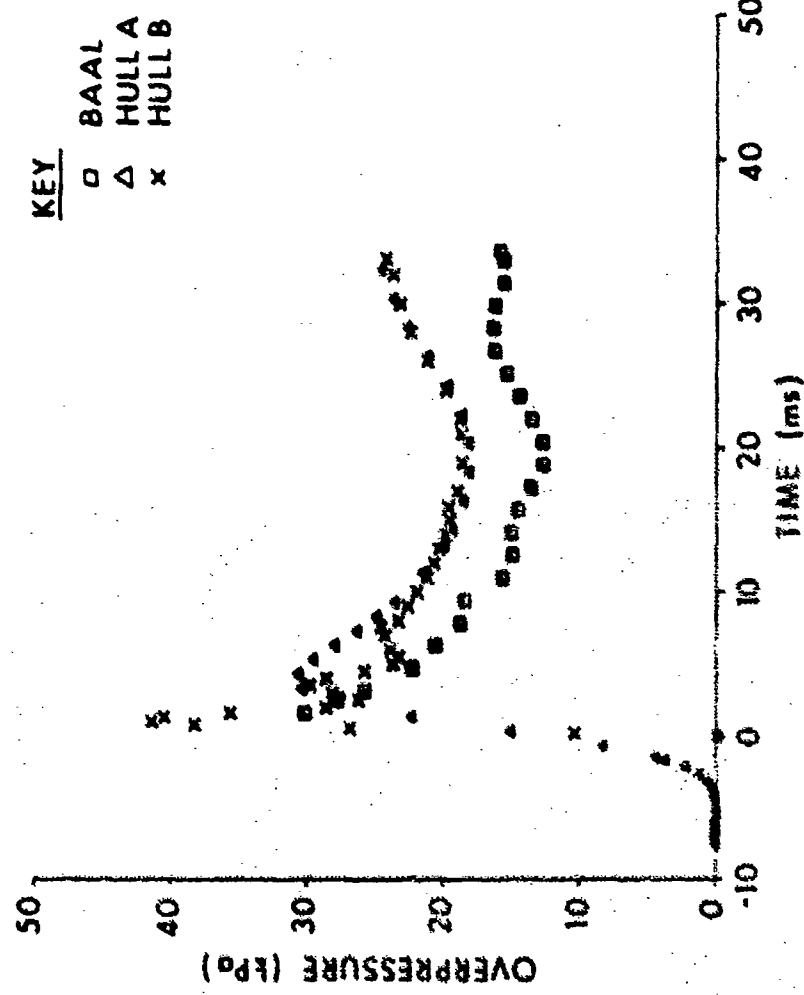


Figure K.11. Overpressure for side face cell (10,8,4).

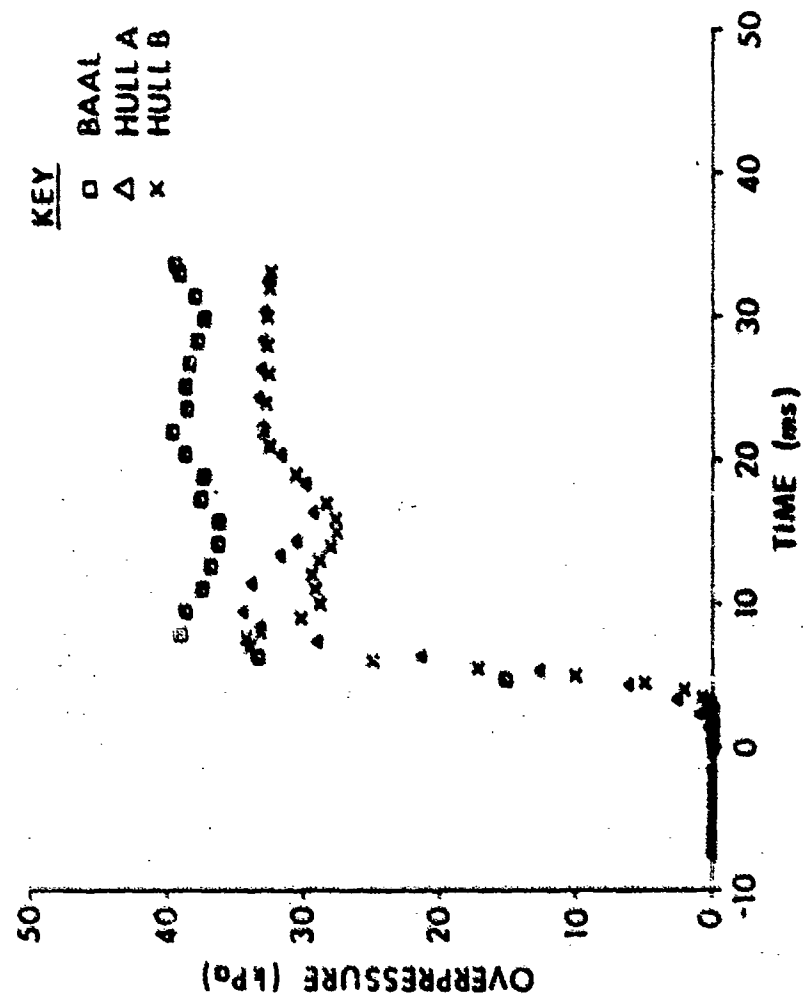


Figure E.12. Overpressure for side face cell (18,8,4).

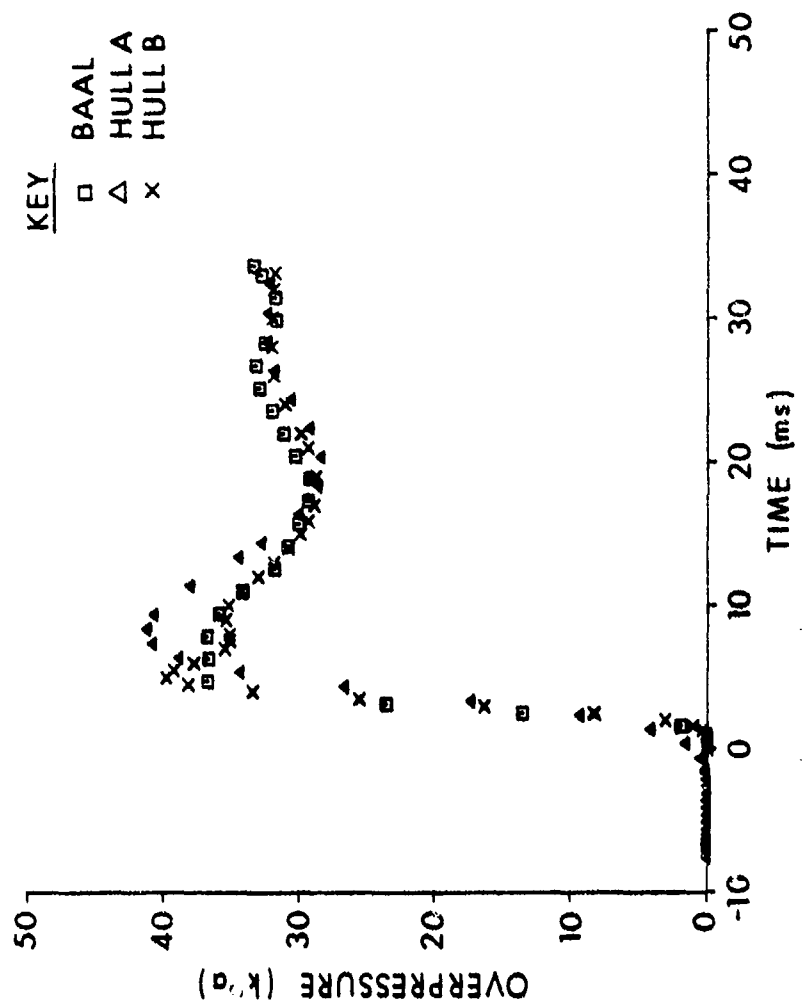


Figure E.13. Overpressure for side face cell (14,8,7).

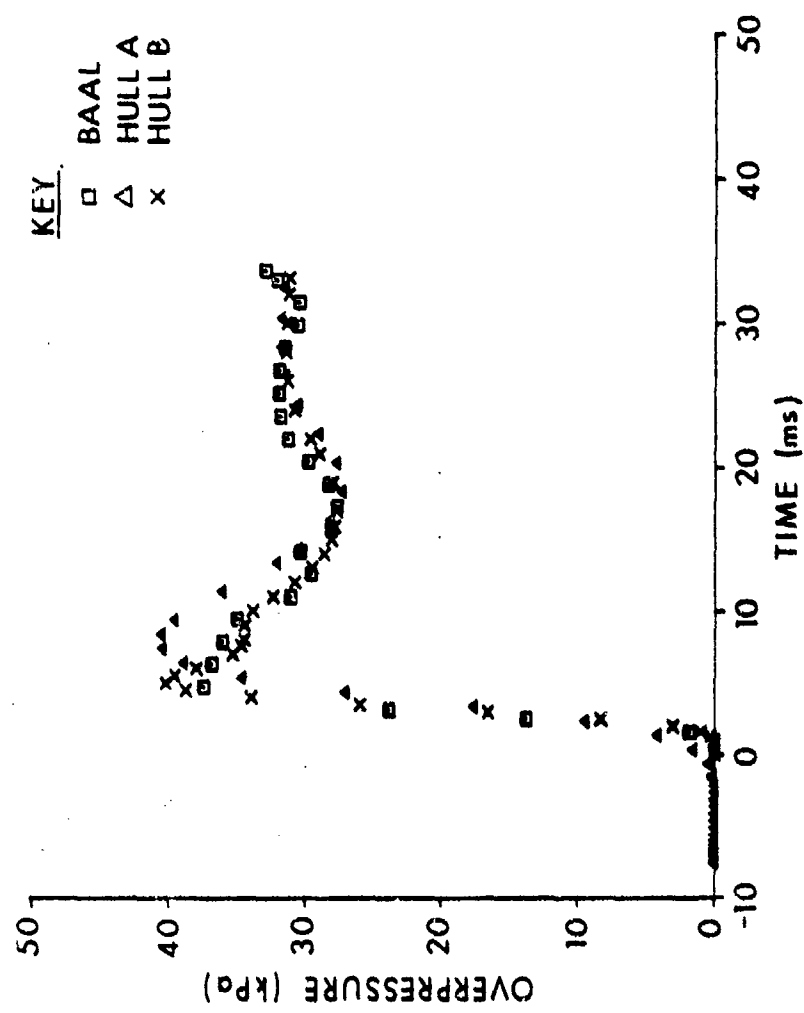


Figure E.14. Overpressure for side face cell (14, 8, 3).

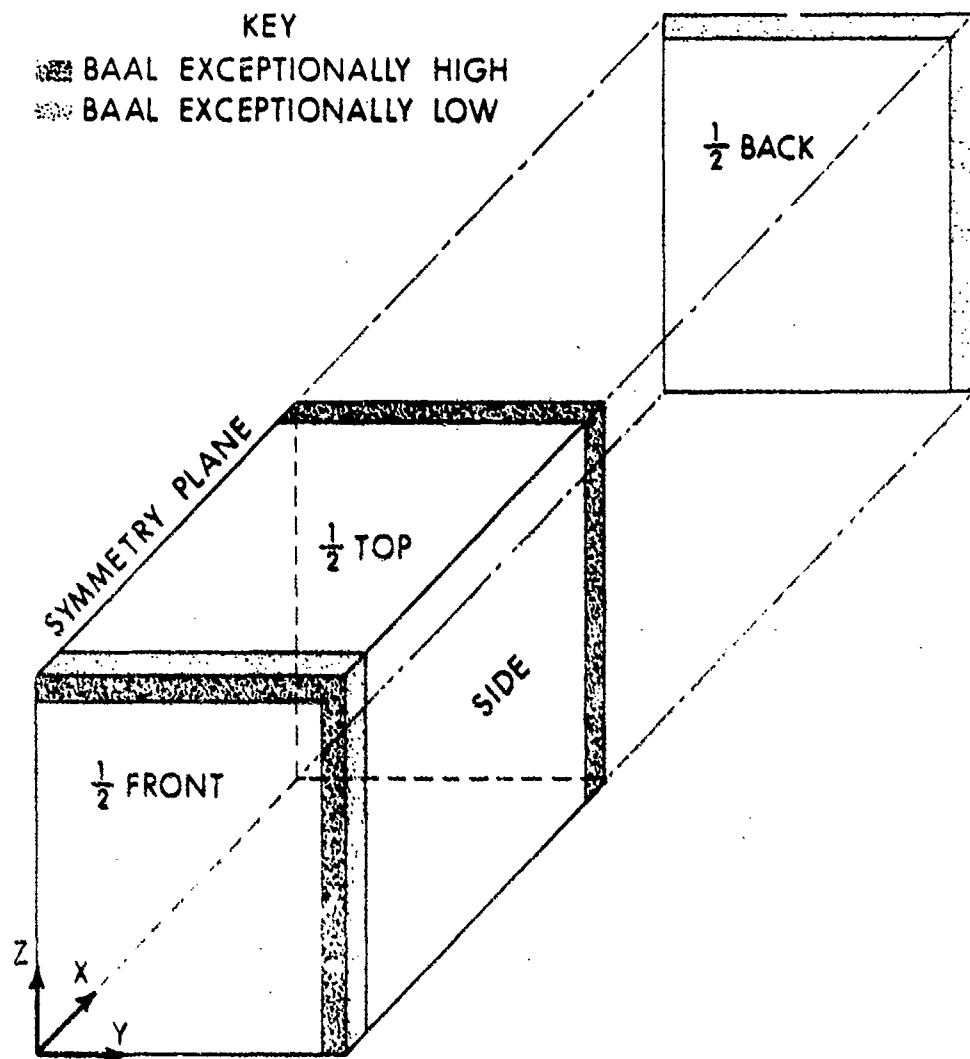


Figure E.15. Exploded view of the S-280 Electrical Equipment Shelter showing flow field cells exhibiting anomalous behavior.

LIST OF SYMBOLS

c	velocity of sound (m/s)
h	the clearing height (m), equal to the smaller of either the height of the target or one-half of its width
p	static, or side-on, pressure (kPa), absolute unless otherwise indicated
t	time (s), where $t = 0.0$ when the incident shock wave arrives at the target front face, as computed according to theory
u	particle velocity (m/s) with respect to an Eulerian reference frame
D	the depth (m) of the target, measured in the direction of travel of the incident shock wave
I	the specific internal energy (J/kg)
M	particle local Mach number
R	gas constant (J/kg-°K)
T	static, or side-on, temperature (°K)
W	wave velocity (m/s) with respect to an Eulerian reference frame
X	the direction of measure of depth (m)
Y	the direction of measure of width (m)
Z	the direction of measure of height (m)
α	a constant multiplicative factor
β	$(p_2 - p_1)/2p_1$
γ	the ratio of specific heats
η	Courant-Friedrichs-Lowy (CFL) stability factor
ρ	static density (kg/m^3), absolute unless otherwise indicated
Subscripts	
b	the back face of the target

LIST OF SYMBOLS (Continued)

c	clearing time when used with the symbol "t", the "... time required to clear the front wall of reflection effects..." ²
drag	the drag phase
f	the front face of the target
i	incident shock wave
max	a peak value
pmin	when used with the symbol "t", the time required for the average pressure on a target face to reach a local minimum value after having been loaded to a peak value by a shock wave
rise	when used with the symbol "t", the time required for a target face to reach a peak average pressure after the initial arrival of the incident wave at that face
top	the top face of the target
0	stagnation, or face-on, value after the flow is isentropically brought to rest
1	ambient, atmospheric, or reference condition, specifically that region of undisturbed gas ahead of the oncoming shock wave
2	the region behind the incident shock wave
3	the region representing the shock tube reservoir
4	the region separated from the shock tube reservoir by the expansion wave, and separated from the shocked gas by the contact discontinuity
5	the region behind the reflected shock wave

Superscripts

- * the value over the reference, or ambient, condition (e.g., p^* represents overpressure)
- average value over a given face of the target

DISTRIBUTION LIST

<u>No. of Copies</u>	<u>Organization</u>	<u>No. of Copies</u>	<u>Organization</u>
12	Commander Defense Technical Info Center ATTN: DDC-DDA Cameron Station Alexandria, VA 22314	1	Director Weapons Systems Evaluation Gp ATTN: Document Control Washington, DC 20305
4	Director of Defense Research and Engineering ATTN: DD/TWP DD/S&SS DD/I&SS AD/SW Washington, DC 20301	1	Director National Security Agency ATTN: E. F. Butala, R15 Ft. George G. Meade, MD 20755
2	Asst. to the Secretary of Defense (Atomic Energy) ATTN: Document Control Donald R. Cotter Washington, DC 20301	3	Director Joint Strategic Target Planning Staff JCS ATTN: Sci & Tech Info Lib JLTW-2 DOXT Offut AFB Omaha, NB 68113
3	Director Defense Advanced Research projects Agency ATTN: Tech Lib NMRO PMO 1400 Wilson Boulevard Arlington, VA 22209	1	Director Defense Communications Agency ATTN: Code 930 Washington, DC 20305
2	Director Federal Emergency Management Agency ATTN: Mr. George Sisson/RF-SR Technical Library Washington, DC 20301	5	Director Defense Nuclear Agency ATTN: STSI/Archives SPAS STSP STVL/Dr. La Vier RATN Washington, DC 20305
4	Director Defense Intelligence Agency ATTN: DT-1B DB-4C/E. O. Farrell DT-2/Wpns & Sys Div RDS-344 Washington, DC 20301	7	Director Defense Nuclear Agency ATTN: DDST/Dr. Conrad DDST/Dr. Oswald STTL/Tech Lib (2 cys) SPSS/K. Goering G. Ullrich SPTD/T. Kennedy Washington, DC 20305

DISTRIBUTION LIST

<u>No. of Copies</u>	<u>Organization</u>	<u>No. of Copies</u>	<u>Organization</u>
2	Commander Field Command, DNA ATTN: FCPR FCTMOF Kirtland AFB, NM 87115	2	Office, Chief of Engineers Department of the Army ATTN: DAEN-MCE-D DAEN-RDM 890 South Pickett Street Alexandria, VA 22304
1	Commander Field Command, DNA Livermore Branch ATTN: FCPR P.O. Box 808 Livermore, CA 94550	5	Commander US Army Engineer Waterways Experiment Station ATTN: Technical Library William Flathau John N. Strange Guy Jackson Leo Ingram P.O. Box 631 Vicksburg, MS 39180
1	Director Institute for Defense Analyses ATTN: IDA Librarian, Ruth S. Smith 400 Army-Navy Drive Arlington, VA 22202	1	Commander US Army Engineering Center ATTN: ATSEN-SY-L Fort Belvoir, VA 22060
1	Program Manager US Army BMD Program Office ATTN: John Shea 5001 Eisenhower Avenue Alexandria, VA 22333	1	Division Engineer US Army Engineering Division ATTN: HNDSE-R/M.M. Dembo Huntsville Box 1600 Huntsville, AL 35804
2	Director US Army BMD Advanced Technology Center ATTN: CRDABH-X CRDABH-S Huntsville, AL 35807	1	Division Engineer US Army Engineering Division Ohio River ATTN: Docu Cen P.O. Box 1159 Cincinnati, OH 45201
1	Commander US Army BMD Command ATTN: BDMSC-1FN/N.J. Hurst P.O. Box 1500 Huntsville, AL 35807	2	HDQA (DAMA-AR; NCL Div) Washington, DC 20310
2	Deputy Chief of Staff for Operations and Plans ATTN: Technical Library Director of Chemical & Nuclear Operations Department of the Army Washington, DC 20310	1	Commander US Army Materiel Development and Readiness Command ATTN: DRCDMD-ST 5001 Eisenhower Avenue Alexandria, VA 22333

DISTRIBUTION LIST

<u>No. of Copies</u>	<u>Organization</u>	<u>No. of Copies</u>	<u>Organization</u>
1	Commander US Army Materiel Development and Readiness Command ATTN: Technical Library 5001 Eisenhower Avenue Alexandria, VA 22333	6	Commander US Army Electronics Research and Development Command ATTN: DELSD-L DELEW-E W. S. McAfee R. Freiberg DELSD-EI, J. Roma DELSD-EM A. Sigismondi C. Goldy Fort Monmouth, NJ 07703
3	Commander US Army Armament Research and Development Command ATTN: DRDAR-LCN-F, W. Reiner DRDAR-TSS (2 cys) Dover, NJ 07801	7	Commander US Army Harry Diamond Labs ATTN: Mr. James Gaul Mr. L. Belliveau Mr. J. Meszaros Mr. J. Gwaltney Mr. F. W. Balicki Mr. Bill Vault Mr. R. J. Bostak 2800 Powder Mill Road Adelphi, MD 20783
1	Commander US Army Armament Materiel Readiness Command ATTN: DRSAR-LEP-L, Tech Lib Rock Island, IL 61299	5	Commander US Army Harry Diamond Labs ATTN: DELHD-TA-L DRXDO-TI/002 DRXDO-NP DRXDO-RBH/P. Caldwell DELHD-RBA/J. Rosado 2800 Powder Mill Road Adelphi, MD 20783
1	Director US Army ARRADCOM Benet Weapons Laboratory ATTN: DRDAR-LCB-TL Watervliet, NY 12189	1	Commander US Army Missile Command ATTN: DRSMI-R Redstone Arsenal, AL 35809
1	Commander US Army Aviation Research and Development Command ATTN: DRDAV-E 4300 Goodfellow Blvd. St. Louis, MO 63120	1	Commander US Army Missile Command ATTN: DRSMI-YG Redstone Arsenal, AL 35809
1	Director US Army Air Mobility Research and Development Laboratory Ames Research Center Moffett Field, CA 94035		
1	Commander US Army Communications Rsch and Development Command ATTN: DRDCO-PPA-SA Fort Monmouth, NJ 07703		

DISTRIBUTION LIST

<u>No. of Copies</u>	<u>Organization</u>	<u>No. of Copies</u>	<u>Organization</u>
2	Commander US Army Missile Command ATTN: MICON-XS/Chief Scientist Technical Library Redstone Arsenal, AL 35809	1	Commander US Army Research Office P.O. Box 12211 Research Triangle Park NC 27709
2	Commander US Army Natick Research and Development Command ATTN: DRXRE/Dr. D. Sieling DRXNM-UE Arthur Johnson Natick, MA 01762	4	Commander US Army Nuclear Agency ATTN: ACTA-NAW MONA-WE Technical Library CPT Ebright 7500 Backlick Rd, Bldg. 2073 Springfield, VA 22150
1	Commander US Army Tank Automotive Rsch and Development Command ATTN: DRDTA-UL Warren, MI 48090	1	Commander US Army TRADOC ATTN: ATCD-SA, Mr. Oscar Wells Fort Monroe, VA 23651
1	Commander US Army Foreign Science and Technology Center ATTN: Rsch & Concepts Branch 220 7th Street, NE Charlottesville, VA 22901	2	Director US Army TRADOC Systems Analysis Activity ATTN: LTC John Hesse ATAA-SL, Tech Lib White Sands Missile Range NM 88002
1	Commander US Army Logistical Center ATTN: ATCL-SCA Mr. Robert Cameron Fort Lee, VA 23801	1	Commander USA Combined Arms Combat Developments Activity ATTN: ATCA-CO, Mr. L.C. Pleger Fort Leavenworth, KS 66027
3	Commander US Army Materials and Mechanics Research Center ATTN: Technical Library John Mescall Richard Shea Watertown, MA 02172	1	Commandant Interservice Nuclear Weapons School ATTN: Technical Library Kirtland AFB, NM 87115
		1	Chief of Naval Material ATTN: MAT 0323 Department of the Navy Arlington, VA 22217

DISTRIBUTION LIST

<u>No. of Copies</u>	<u>Organization</u>	<u>No. of Copies</u>	<u>Organization</u>
2	Chief of Naval Operations ATTN: OP-05EG OP-985F Department of the Navy Washington, DC 20350	2	Commander Naval Ship Engineering Ctr ATTN: Technical Library NSEC 6105G Hyattsville, MD 20782
1	Chief of Naval Research ATTN: N. Perrone Department of the Navy Washington, DC 20360	1	Commander David W. Taylor Naval Ship Research & Development Ctr ATTN: Lib Div, Code 522 Bethesda, MD 20084
3	Director Strategic Systems Projects Ofc ATTN: NSP-43, Tech Lib NSP-273 NSP-272 Department of the Navy Washington, DC 20360	1	Commander Naval Surface Weapons Center ATTN: DX-21, Library Br. Dahlgren, VA 22448
1	Commander Naval Electronic Systems Com ATTN: PME 117-21A Washington, DC 20360	3	Commander Naval Surface Weapons Center ATTN: Code WAS01/Navy Nuclear Programs Office Code WX21/Tech Lib Code 240/C.J. Aronson Silver Spring, MD 20910
3	Commander Naval Facilities Engineering Command ATTN: Code 03A Code 04A Technical Library Washington, DC 20360	2	Commander Naval Weapons Center ATTN: Code 553, Tech Lib Code 55804, M. Keith China Lake, CA 93555
2	Commander Naval Sea Systems Command ATTN: ORD-91313 Library Code 03511 Department of the Navy Washington, DC 20362	2	Commander Naval Ship Research and Development Center Facility Underwater Explosions Research Division ATTN: Code 17, W.W. Murray Technical Library Portsmouth, VA 23709
4	Officer-in-Charge Civil Engineering Laboratory Naval Constr Bn Ctr ATTN: Stan Takahashi R. J. Odello John Crawford Technical Library Port Hueneme, CA 93041	2	Commander Naval Weapons Evaluation Facility ATTN: Document Control R. Hughes Kirtland AFB Albuquerque, NM 87117

DISTRIBUTION LIST

<u>No. of Copies</u>	<u>Organization</u>	<u>No. of Copies</u>	<u>Organization</u>
1	Commander Naval Research Laboratory ATTN: Code 2027, Tech Lib Washington, DC 20375	1	AFWL/SUL, Jimmie L. Bratton Kirtland AFB, NM 87117
1	Superintendent Naval Postgraduate School ATTN: Code 2124 Tech Reports Lib Monterey, CA 93940	1	AFWL/R. Henny Kirtland AFB, NM 87117
1	HQ USAF (IN) Washington, DC 20330	1	AFWL/SUL, M. A. Plamondon Kirtland AFB, NM 87117
1	HQ USAF (PRE) Washington, DC 20330	2	Commander-in-Chief Strategic Air Command ATTN: NRI-STINFO Lib SPFS Offutt AFB, NB 68113
2	AFSC (DLCAW; Tech Lib) Andrews AFB Washington, DC 20331	1	AFIT (Lib Bldg. 640, Area B) Wright-Patterson AFB Ohio 45433
2	ADTC (ADBRL-2; Tech Lib) Eglin AFB, FL 32542	4	FTD (TDFBD; TDPMG: ETET, CPT R.C. Husemann: TD/BTA/Lib) Wright-Patterson AFB Ohio 45433
2	AFATL (DLYV, P. Nash) Eglin AFB, FL 32542	1	Director US Bureau of Mines ATTN: Technical Library Denver Federal Center Denver, CO 80225
1	AFATL (DLYV, Jim Flint) Eglin AFB, FL 32542	1	Director US Energy Research and Development Administration Albuquerque Operations Office ATTN: Document Control for Tech Lib P. O. Box 5400 Albuquerque, NM 87115
3	RADC (EMTLD/Docu Lib; ENREC/R.W. Mair) Griffiss AFB, NY 13340		
1	AFWL/DE-I Kirtland AFB, NM 87117		
1	AFWL/DEX Kirtland AFB, NM 87117		

DISTRIBUTION LIST

<u>No. of Copies</u>	<u>Organization</u>	<u>No. of Copies</u>	<u>Organization</u>
1	Director Lawrence Livermore Lab ATTN: L.W. Woodruff/L-96 P.O. Box 808 Livermore, CA 94550	4	Director Los Alamos Scientific Lab ATTN: Doc Control for Rpts Lib R. A. Gentry G. R. Spillman Al Davis P.O. Box 1663 Los Alamos, NM 87544
1	Director Lawrence Livermore Lab ATTN: Jack Kahn/L-7 P.O. Box 808 Livermore, CA 94550	1	US Energy Research and Development Administration Nevada Operations Office ATTN: Doc Control for Tech Lib P.O. Box 14100 Las Vegas, NV 89114
1	Director Lawrence Livermore Lab ATTN: Tech Info Dept L-3 P.O. Box 808 Livermore, CA 94550	6	Sandia Laboratories ATTN: Doc Control for 3141 Sandia Rpt Collection A. M. Chaban M. L. Merritt L. J. Vortman W. Roherty L. Hill P.O. Box 5800 Albuquerque, NM 87115
1	Director Lawrence Livermore Lab ATTN: Ted Butkovich/L-200 P.O. Box 808 Livermore, CA 94550	1	Sandia Laboratories Livermore Laboratory ATTN: Doc Control for Tech Lib P.O. Box 969 Livermore, CA 94550
1	Director Lawrence Livermore Lab ATTN: Robert Schock/L-437 P.O. Box 808 Livermore, CA 94550	1	Director National Aeronautics and Space Administration Scientific and Technical Information Facility P.O. Box 8757 Baltimore/Washington International Airport, MD 21240
1	Director Lawrence Livermore Lab ATTN: J. R. Hearst/L-205 P.O. Box 808 Livermore, CA 94550		

DISTRIBUTION LIST

<u>No. of Copies</u>	<u>Organization</u>	<u>No. of Copies</u>	<u>Organization</u>
3	Aerospace Corporation ATTN: Tech Info Services (2 cys) P. N. Mathur P.O. Box 92957 Los Angeles, CA 90009	2	California Research and Technology, Inc. ATTN: Ken Kreyenhagen Technical Library 6929 Variel Avenue Woodland Hills, CA 91364
1	Agbabian Associates ATTN: M. Agbabian 250 North Nash Street El Segundo, CA 90245	1	Calspan Corporation ATTN: Technical Library P.O. Box 400 Buffalo, NY 14221
1	Applied Theory, Inc. ATTN: John G. Trulio 1010 Westwood Blvd. Los Angeles, CA 90024	1	Civil/Nuclear Systems Corp ATTN: Robert Crawford 1200 University N.E. Albuquerque, NM 87102
1	Artec Associates, Inc. ATTN: Steven Gill 26046 Eden Landing Road Hayward, CA 94545	1	EG&G, Incorporated Albuquerque Division ATTN: Technical Library P.O. Box 10218 Albuquerque, NM 87114
1	AVCO ATTN: Res Lib A830, Rm 7201 201 Lowell Street Wilmington, MA 01887	1	The Franklin Institute ATTN: Lemons Ludans 20th Street and Parkway Philadelphia, PA 19103
1	The BDM Corporation ATTN: Richard Hensley P.O. Box 9274 Albuquerque International Albuquerque, NM 87119	3	General American Trans Corp General American Research Div ATTN: G. L. Neidhardt M. R. Johnson 7449 N. Natchez Avenue Niles, IL 60648
2	The Boeing Company ATTN: Aerospace Library R. H. Carlson P.O. Box 3707 Seattle, WA 98124	1	General Electric Company-TEMPO ATTN: OASIA P.O. Drawer QO Santa Barbara, CA 93102

DISTRIBUTION LIST

<u>No. of Copies</u>	<u>Organization</u>	<u>No. of Copies</u>	<u>Organization</u>
1	Kaman-TEMPO ATTN: E. Bryant, Suite UL-1 715 Shamrock Road Bel Air, MD 21014	2	Martin Marietta Aerospace Orlando Division ATTN: G. Fotieo Mail Point 505, Craig Luongo P.O. Box 5837 Orlando, FL 32805
2	Hazeltine Corp. ATTN: Carl Meinen Greenlawn, NY 11740	3	McDonnell Douglas Astronautics Corporation ATTN: Robert W. Halprin Mr. C. Gardiner Dr. P. Lewis 5301 Bolsa Avenue Huntington Beach, CA 92647
1	J. H. Wiggins Co., Inc. ATTN: John Collins 1650 South Pacific Coast Highway Redondo Beach, CA 90277	2	Merrity Cases, Inc. ATTN: J. L. Merritt Technical Library P.O. Box 1206 Redlands, CA 92373
5	Kaman AviDyne ATTN: Dr. N.P. Hobbs (4 cys) Mr. S. Criscione 83 Second Avenue Northwest Industrial Park Burlington, MA 01830	1	Netecology Research, Inc. ATTN: W. D. Green 454 West Woodbury Road Altadena, CA 91001
3	Kaman Sciences Corporation ATTN: Library P. A. Ellis F. H. Shelton 1500 Garden of the Gods Road Colorado Springs, CO 80907	1	The Mitre Corporation ATTN: Library P.O. Box 208 Bedford, MA 01730
1	Kaman Sciences Corporation ATTN: Don Sachs Suite 703 2001 Jefferson Davis Highway Arlington, VA 22202	1	Pacific Sierra Research Corp ATTN: Dr. Harold Brode 1456 Cloverfield Boulevard Santa Monica, CA 90404
1	Lockheed Missiles & Space Co. ATTN: Technical Library P.O. Box 504 Sunnyvale, CA 94088	2	Pacifica Technology ATTN: G. Kent R. Bjork P.O. Box 148 Del Mar, CA 92014

DISTRIBUTION LIST

<u>No. of Copies</u>	<u>Organization</u>	<u>No. of Copies</u>	<u>Organization</u>
5	Physics International Corp ATTN: Robert Swift Charles Godfrey Larry A. Behrmann Fred Sauer Technical Library 2700 Merced Street San Leandro, CA 94577	2	Science Applications, Inc. ATTN: Technical Library Michael McKay P.O. Box 2351 La Jolla, CA 92038
3	R&D Associates ATTN: Dr. Albert L. Latter William B. Wright A. Kuhl P.O. Box 9695 Marina del Rey, CA 90291	1	Science Systems and Software ATTN: C. E. Needham P.O. Box 8243 Albuquerque, NM 87198
4	R&D Associates ATTN: Jerry Carpenter Sheldon Schuster J. G. Lewis Technical Library P.O. Box 9695 Marina del Rey, CA 90291	1	Systems, Science & Software ATTN: Donald R. Grine Ted Cherry Thomas D. Riney Technical Library P.O. Box 1620 La Jolla, CA 92037
1	R&D Associates Suite 500 1401 Wilson Boulevard Arlington, VA 22209	3	Terra Tek, Inc. ATTN: Sidney Green A. H. Jonas Technical Library 420 Wakara Way Salt Lake City, UT 84108
1	The Rand Corporation ATTN: C. C. Now 1700 Main Street Santa Monica, CA 90406	2	Tetra Tech, Inc. ATTN: Li-San Hwang Technical Library 650 North Rosemead Blvd. Pasadena, CA 91107
2	Science Applications, Inc. ATTN: Bert Chambers John Cockayne 8400 Westpart Drive McLean, VA 22102	7	TRW Systems Group ATTN: Paul Lieberman Benjamin Sussolitz Norm Lipner William Rowan Jack Farrell Pravin Bhutta Tech Info Ctr/S-1930 One Space Park Redondo Beach, CA 92078
1	Science Applications, Inc. 2450 Washington Avenue Suite 120 San Leandro, CA 94577		

DISTRIBUTION LIST

<u>No. of Copies</u>	<u>Organization</u>	<u>No. of Copies</u>	<u>Organization</u>
1	TRW Systems Group ATTN: Greg Hulcher San Bernardino Operations P.O. Box 1310 San Bernardino, CA 92402	2	Denver Research Institute University of Denver ATTN: Mr. J. Wisotski Technical Library P.O. Box 10127 Denver, CO 80210
2	Union Carbide Corporation Holifield National Laboratory ATTN: Doc Control for Tech Lib Civil Defense Research Proj P.O. Box X Oak Ridge, TN 37830	3	IIT Research Institute ATTN: Milton R. Johnson R. E. Welch Technical Library 10 West 35th Street Chicago, IL 60616
1	Universal Analytics, Inc. ATTN: E. I. Field 7740 W. Manchester Blvd. Playa del Rey, CA 90291	2	Lovelace Foundation for Medical Education ATTN: Asst. Dir of Research/ Robert K. Jones Technical Library 5200 Gibson Blvd., SF Albuquerque, NM 87109
1	Weidlinger Assoc. Consulting Engineers ATTN: M. L. Baron 110 East 59th Street New York, NY 10022	1	Massachusetts Institute of Technology Aeroelastic and Structures Research Laboratory ATTN: Dr. E. A. Witmer Cambridge, MA 02139
1	Westinghouse Electric Co. Marine Division ATTN: W. A. Votz Hendy Avenue Sunnyvale, CA 94008	2	Southwest Research Institute ATTN: Dr. W. E. Baker A. B. Wenzel 9500 Culebra Road San Antonio, TX 78206
2	Battelle Memorial Institute ATTN: Technical Library R. W. Klingensmith 505 King Avenue Columbus, OH 43201	2	SRI International ATTN: Dr. G. R. Abrahamson Carl Peterson 333 Ravenswood Avenue Menlo Park, CA 94035
1	California Institute of Technology ATTN: T. J. Ahrens 1201 E. California Blvd. Pasadena, CA 91109		

DISTRIBUTION LIST

<u>No. of</u>	<u>Copies</u>	<u>Organization</u>
1		University of Dayton Industrial Security Super. KL-505 ATTN: H. F. Swift 300 College Park Avenue Dayton, OH 45409
1		University of Illinois Consulting Engineering Services ATTN: Nathan M. Newmark 1211 Civil Engineering Bldg Urbana, IL 61801
2		The University of New Mexico The Eric H. Wang Civil Engineering Research Facility ATTN: Larry Bickle Neal Baum University Station Box 188 Albuquerque, NM 87131
2		Washington State University Administration Office ATTN: Arthur Miles Mohorf George Duval Pullman, WA 99163

Aberdeen Proving Ground

Dir, USAMSAA
ATTN: DRXSY-D
DRXSY-MP, H. Cohen
Cdr, USATECOM
ATTN: DRSTE-TO-F
Dir, USACSL
Bldg. E3516, EA
ATTN: DRDAR-CLB-PA